J. Fluid Mech. (2005), *vol.* 535, *pp.* 143–188.
doi:10.1017/S0022112005004751 Printed in the United Kingdom

Experimental study of eddy structures in a turbulent boundary layer using particle image velocimetry

By JOHAN CARLIER AND MICHEL STANISLAS

Laboratoire de Mécanique de Lille, Boulevard Paul Langevin, 59655 Villeneuve d'Ascq, France

(Received 12 December 2002 and in revised form 24 November 2004)

Particle image velocimetry experiments have been performed in a turbulent boundary-layer wind tunnel in order to study the coherent structures taking part in the generation and preservation of wall turbulence. The particular wind tunnel used is suitable for high-resolution experiments ($\delta > 0.3\,\mathrm{m}$) at high Reynolds numbers (up to $R_\theta = 19\,000$ in the present results). Eddy structures were identified in instantaneous velocity maps in order to determine their mean characteristics and possible relationships between these structures. In the logarithmic region, the results show that the observed eddy structures appear to organize like elongated vortices, tilted downstream, mainly at an angle of about 45° and having a cane shape. The characteristics of these vortices appear here to be universal in wall units for $R_\theta \leqslant 19\,000$. They seem to find their origin at a wall distance of about 25 wall units as quasi-streamwise vortices and to migrate away from the wall while tilting to form a head and a leg. Away from the wall, their radius increases and their vorticity decreases very slowly so that their circulation is nearly constant. Near the wall, the picture obtained is in fair agreement with existing models. The analysis of the results indicates a universality of the buffer-layer mechanism, even at low Reynolds number, and a sensitivity of the logarithmic region to low-Reynolds-number effects.

1. Introduction

Turbulence is often regarded as a superposition of interacting eddy structures with a whole spectrum of sizes. If they may be considered as diffusive and dissipative, some of these structures are also known to be productive of turbulent stresses, owing, for example, to interaction with shear. This is the case for those which take part in the generation and preservation of wall turbulence by interacting with the wall, or with neighbouring coherent structures. In wall turbulence, such active eddy structures have been mainly identified as 'hairpin vortices' and 'streamwise vortices', but other proposals exist, such as 'typical eddies', for example.

Theodorsen (1952) was the first to suggest the existence of horseshoe vortices (see figure 1) in wall turbulence by considering the transport equations of the vorticity ($\boldsymbol{\omega} = \mathrm{rot}\boldsymbol{v}$). Their origin would be the instability of the instantaneous velocity profile evolving into transverse vortices. They are supposed to be tilted at about 45° downstream, owing mainly to the mean velocity gradient which stretches them and to the mechanism of self-induction which lifts them up. Townsend (1976) added to this description the 'attached-eddy hypothesis' in which the legs of horseshoe vortices would remain attached to the wall during their development. The mean

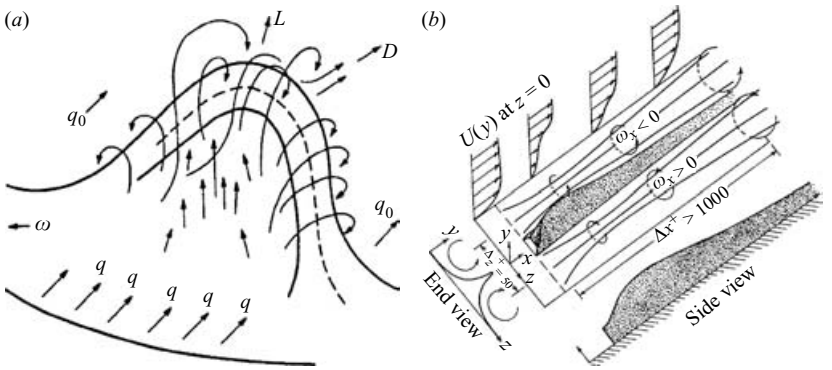

FIGURE 1. (*a*) Horseshoe vortex by Theodorsen (1952); (*b*) counter-rotating pairs of streamwise vortices by Blackwelder & Kaplan (1976).

spacing between these legs is about 100 wall units (which will be noted 100^+ hereinafter for the sake of compactness), but the aspect ratio of the horseshoe vortices is Reynolds-number dependent (see Head & Bandyopadhyay 1981). Indeed, these eddy structures appear more elongated at higher Reynolds number and are then called hairpin vortices. Robinson (1991) detected them using a pressure criteria in the direct numerical simulation (DNS) of a flat-plate boundary layer by Spalart (1988). He noticed that these hairpin vortices generally appear more asymmetric than sketched in the literature, having more of a cane shape (with two legs of different lengths) than the usual symmetric hairpin shape put forward by most previous authors.

Using hydrogen bubbles, Kim, Kline & Reynolds (1971) observed near the wall a rotational motion which they interpreted as streamwise vortices. However, the mechanisms of formation of these eddy structures are not yet well understood. A popular theory is that streamwise vortices are the legs near the wall of the hairpin vortices previously described. One other proposal is that streamwise vortices are secondary vortices in the trailing legs near the wall of these hairpin vortices. Based on the conditional analysis of hot-film signals, Blackwelder & Eckelmann (1979) inferred that streamwise vortices evolve by counter-rotating pairs near the wall (see figure 1). Their centres are located at about 25^+ from the wall and are separated by 50^+ to 100^+ in the transverse direction; their radius is about 15^+ and their length of the order of 200^+. Kim, Moin & Moser (1987) found nearly the same sizes by the analysis of the vorticity fluctuation profiles in a DNS of a turbulent channel flow. However, Robinson (1991) found very few streamwise vortices in the counter-rotating configuration.

In the concept of self-sustaining wall turbulence, these two kinds of eddy structure interact with other types of inner-layer coherent structures among which 'low and high speed streaks' and 'sweeps and ejections' are the most documented.

Low- and high-speed streaks were discovered by Kline *et al.* (1967) by showing that hydrogen bubbles introduced close to the wall concentrate into wavy streamwise stripes. Since this discovery, many authors have observed them and a consensus about their characteristics has emerged (except for the streamwise extent, on which opinions vary widely). Low-speed streaks appear under 10^+ where they are relatively quiet. They are between 500^+ and 2000^+ in length, between 20^+ and 40^+ in width and between 5^+ and 10^+ in height. They are separated by a distance varying widely between 50^+ and 300^+ in the transverse direction. These dimensions increase when they become suddenly very active, lifting up toward the buffer layer. Blackwelder & Eckelmann (1979) proposed that the low-speed streaks come from counter-rotating

pairs of streamwise vortices, which lift up low-velocity fluid from the wall. Another proposal is that the low-speed streaks are the trace of one or several stacked hairpin vortices, flying over the wall, which lift up, between their legs and under their heads, low-speed fluid from the wall. These eddy structures then extend along the downstream part of a low-speed streak. The two proposals agree if it is considered that counter-rotating pairs of streamwise vortices are legs near the wall of the hairpin vortices. For both types of coherent structure, symmetry is not a necessary condition to the formation of low-speed streaks.

From high-speed imaging of a flow seeded with solid particles in suspension, Corino & Brodkey (1969) identified the two events which take part in the production of turbulence close to the wall. The first event is ejection of low-velocity fluid called simply 'ejection'. The lift-up of the low-speed streaks is generally made responsible for the formation of these ejections. This process is at the heart of wall turbulence dynamics. The second event is high-velocity fluid sweeping down to the wall and called simply 'sweep'. The existence of the latter can be justified by the necessary conservation of mass induced by the ejections.

The relation between all these coherent structures leading to an explanation of the self-sustaining mechanism of near-wall turbulence has been the subject of detailed investigation by many workers (see, for example, Panton 1997), but the picture that has emerged is not altogether clear and this research subject is still very active. If the main coherent structures of wall turbulence have now been described in detail, the mechanisms responsible for their formation and their contribution to the generation and the preservation of wall turbulence are not yet well established. In a classically admitted scenario going back to Theodorsen (1952), the instability of the longitudinal instantaneous velocity profile is supposed to be the source of creation of transverse vortices. Under the action of the mean velocity gradient and the three-dimensional character of the flow, these transverse vortices evolve rapidly into deformed vortex tubes, looking like streamwise or hairpin vortices. Both vortical structures explain the formation of the low-speed streaks close to the wall. These low-speed streaks seem to be at the origin of the above-mentioned instability, through what is called the ejection and bursting process in the buffer layer. The bursts, which look like hairpin packets, grow to become turbulent bulges in the outer part of the turbulent boundary layer. This bursting process generally consists of several ejections (and vortices), responsible for the mass transfer away from the wall. This outward mass transfer is necessarily compensated by sweep motions toward the wall. The result of these two events occurring close to the wall is a strong production of turbulence in this region. This wall-generated turbulence is then diffused away and dissipated slowly in the turbulent bulges. In the concept of a regeneration cycle of turbulence, the production of new vortical structures is at present attributed either to the instability of the instantaneous velocity profile due to the streaks, or to an induction mechanism by the already existing vortices. Some authors invoke both mechanisms. At low Reynolds number, Jiménez & Pinelli (1999) have shown by DNS that the self-sustaining of wall turbulence appears to be local to the near-wall region and does not depend strongly on the outer part. Essentially, it involves vortical structures (which play a central role), low-speed streaks and ejections. The question of whether this is also true at high Reynolds number is still open.

The existence of vortical structures in wall turbulence is not in any doubt. However, the distinction between the various forms suggested is not observed clearly by visualization or numerical methods, especially at high Reynolds numbers (most of the studies mentioned above were performed at fairly low Reynolds

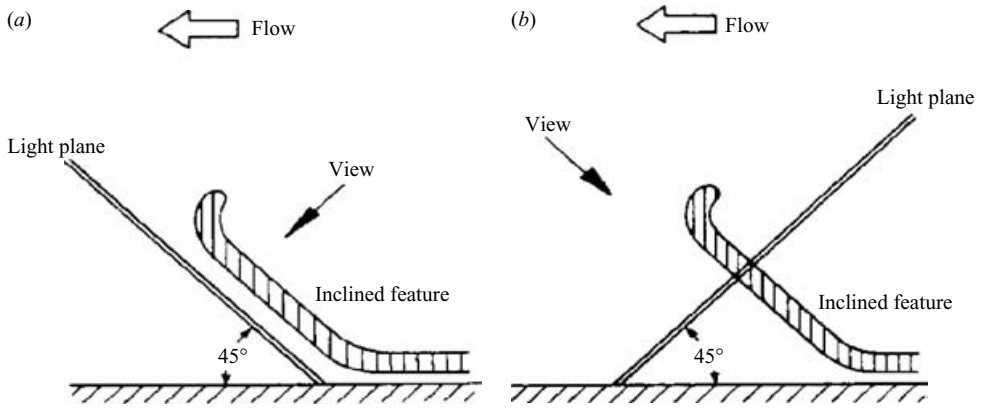

FIGURE 2. Hairpin vortices and inclined planes by Head & Bandyopadhyay (1981). (*a*) Downstream tilted plane, (*b*) upstream tilted plane.

number). Nevertheless, Head & Bandyopadhyay (1981) were the first to carry out original visualization experiments of boundary layers over a large Reynolds number range $500 < R_\theta < 17\,500$. They provided images obtained with various light-sheet configurations which appeared to cut, or not, the axis of the vortex tubes depending on the orientation of the light sheet. The selected configurations were a longitudinal plane normal to the wall and two transverse planes inclined, respectively, at an angle of 45° upstream and 45° downstream (see figure 2). They concluded that hairpin vortices are the major components of a turbulent boundary layer at all Reynolds numbers. Unfortunately, details of the flow in the immediate vicinity of the wall could not be distinguished readily with this visualization technique. Consequently, the formation of hairpin vortices could not be connected directly with events occurring in the buffer layer, and streamwise vortices could not be identified in the near-wall region.

Owing to technical progress, particle image velocimetry (PIV) has developed rapidly in the last ten years and is now a widely used technique for investigations where the spatial distribution of the velocity helps us to understand the physics of the flow, see Adrian (1991). Although it is not yet well time-resolved, this technique, by providing a large number of accurate velocity maps with a high spatial resolution, is mature enough to assess coherent structures in turbulent flows. The aim of the present contribution was thus to use PIV in the same light-sheet configurations as in the study by Head & Bandyopadhyay (1981) in order to assess quantitatively the coherent structures and, particularly, the eddy structures pointed out by them.

Adrian and colleagues at Urbana Champaign has also started to study wall turbulence with PIV. Several experiments were carried out at Reynolds numbers R_θ ranging between 930 and 6845 with different methods: classical 2D2C (two spatial dimensions and two velocity components) by Meinhart & Adrian (1995), translation 2D3C (two spatial dimensions and three velocity components) by Liu *et al.* (1996) and angular 2D3C by Kähler, Adrian & Willert (1998). Instantaneous velocity fields were obtained in a streamwise plane normal to the wall. These allowed the profiles of the mean velocity and Reynolds stress tensor components to be measured. Moreover, these measurements allowed the computation of the double spatial correlation coefficients of the velocity (see Liu, Adrian & Hanratty 2001). In addition to this statistical analysis, a phenomenological analysis of instantaneous velocity maps was also conducted in order to identify some coherent structures such as sweeps, ejections and eddy

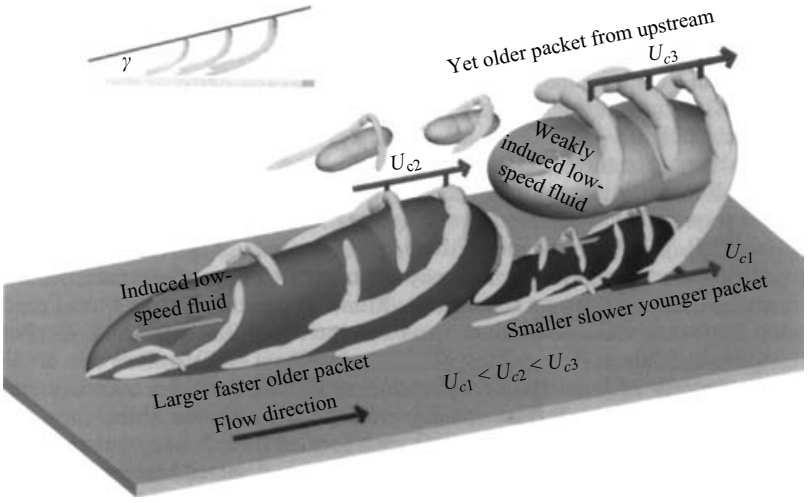

FIGURE 3. Conceptual model of the organization of turbulence close to the wall proposed by Adrian *et al.* (2000*b*).

structures. Attention was focused particularly on the impact of eddy structures on the spatial organization of the wall turbulence. DNS of the evolution of one hairpin vortex in a turbulent channel flow was carried out at a Reynolds number R_θ of 280. By visualizing the eddy structures from the fields of the complex part of one of the eigenvalues of the gradient tensor (λ_2 criterion), Zhou *et al.* (1999) showed that the initial hairpin vortex persists in time. It induces, upstream and downstream, other hairpin vortices associated with ejections. This system of hairpin vortices generates progressively a low-speed streak. The envelope of this vortical system is tilted at an angle to the wall of 10° to 15° on its upstream side and 7° to 15° on its downstream side. Adrian, Meinhart & Tomkins (2000*b*) deduce from both experimental and numerical studies, a conceptual model of the organization of turbulence near the wall reproduced in figure 3. This model is based on the notion of 'hairpin packets' and synthesizes the knowledge at the time of writing, taking its roots in the pictures proposed, among others, by Hinze (1975) and Acarlar & Smith (1987).

In addition to the analysis of Adrian in the longitudinal plane normal to the wall, results are presented here from the authors' PIV experiments in two transverse planes inclined at an angle of 45° upstream and 45° downstream. Moreover, one configuration was added, in which stereoscopic PIV was used in a plane normal to the flow. The range of Reynolds number R_θ covered is from 7500 to 19 000. The region of investigation covers the buffer layer and part of the logarithmic region. Eddy structures are detected in the velocity maps using an identification method based on pattern recognition. The characteristics of the eddy structures detected are determined by fitting them with an Oseen vortex model. Possible relationships between eddy structures and other coherent structures such as low-speed streaks or ejections and sweeps are determined by cross-correlating indicative functions of the regions which they occupy in the velocity maps.

2. Experimental facility description and characterization

In this section, the specific wind tunnel used and the hot-wire experiments carried out to characterize the boundary layer (BL) are described. Then, the main results of

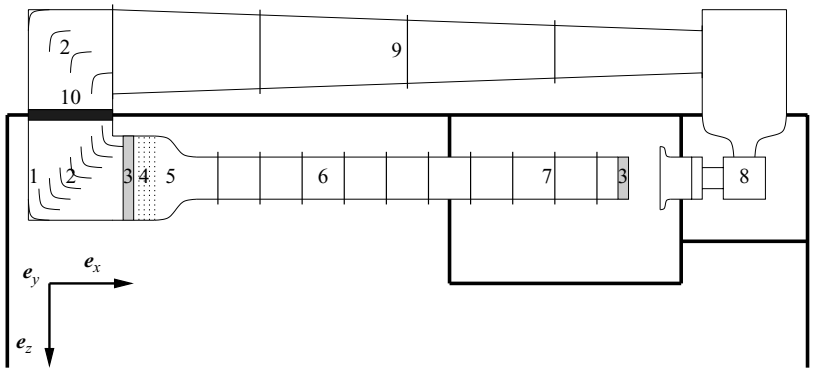

FIGURE 4. Sketch of the top view of the wind tunnel: 1, plenum chamber; 2, guide vanes; 3, honeycomb; 4, grids; 5, contraction; 6, turbulent boundary layer developing zone; 7, testing zone of wind tunnel; 8, fan and motor; 9, return circuit; 10, heat exchanger (air–water).

this hot-wire study are presented and discussed. In the present paper, $[\cdots]^+$ are wall units based on the wall friction velocity u_τ and the viscosity ν. $[\cdots]^\times$ are based on the external velocity U_e and the BL thickness δ.

2.1. *Boundary-layer wind tunnel*

This facility is suitable for high-resolution experiments at high Reynolds numbers. In the case of a turbulent boundary layer along a flat plate, the Reynolds number based on the momentum thickness R_θ can reach 20 600 (19 000 in the present PIV experiments), with a boundary-layer thickness δ of about 0.3 m.

Figure 4 presents a sketch of the top view of the wind tunnel. The longitudinal axis x is parallel to the wall and to the flow, the normal axis y is normal to the wall and the transverse axis z is such that the reference frame is direct. A large plenum chamber with guide vanes followed by a honeycomb, grids and a contraction decrease the turbulence level to about 0.3 % of the external velocity U_e at the entrance of the wind tunnel. This wind tunnel is $1 \times 2\,\mathrm{m}^2$ in cross-section and 21.6 m in length. Transparent walls are used along the last 5 m of the working section on all sides to allow the use of optical methods. A return circuit is used to ensure a good control of the flow parameters. The temperature is kept within ± 0.2 K by using an air–water heat exchanger located in the plenum chamber. The external velocity in the testing zone of the wind tunnel can be chosen continuously from 3 to $10\,\mathrm{m\,s}^{-1}$ with a stability better than 0.5 % by varying the fan rotation speed. Both parameters are fully computer controlled during the hot-wire measurements.

The boundary layer under study develops over the lower flat wall of the wind tunnel. It is tripped by a grid fixed on the floor at the entrance of the developing zone. This grid fixes the BL transition and increases slightly the BL thickness in the test section. Its dimensions are a length of 2 m, a thickness of 5 mm and a grid spacing of 10 cm.

The turbulent statistics are not affected by the tripping grid (except for the BL thickness δ which increases by about 12 % in the test section). This was checked carefully by comparing results from hot-wire anemometry (HWA) experiments achieved with and without the grid.

Corner effects due to the rectangular cross-section of the wind tunnel do not affect the homogeneity of the flow in the transverse direction up to ± 35 cm from the vertical

plane of symmetry of the tunnel. This point was checked by comparing results from HWA experiments achieved at three transverse positions ($z = 0$, + and − 35 cm).

The walls of the wind tunnel are parallel. This establishes a streamwise pressure gradient in the wind tunnel (see § 2.3). This pressure gradient, scaled in wall units $[(1/\rho)P_{,x}]^+$, varies between 0.14 and 0.51 10^{-3}. This can be considered as low in the Navier–Stokes equations for the present case (see Mellor 1966). In external scaling $K = [(\nu/U_e{}^2)U_{e,x}]$, the pressure gradient varies between 6×10^{-9} and 2.5×10^{-8}. This again is considered as negligeable (see DeGraaff & Eaton 2000).

2.2. *Hot-wire anemometry*

The turbulent characteristics of the boundary layer have been investigated in detail with HWA, using single and X-wires. The hot-wire probes used were specially manufactured by AUSPEX. They are of boundary-layer type to approach the wall at best. The wires are made of platinium plated tungsten. They are 2.5 μm in diameter. The wire is 0.5 mm long for single wires and 0.7 mm for X-wires. The spacing of X-wire prongs is 0.5 mm (which vary between 4^+ and 12^+ depending on the Reynolds number).

The anemometers used are of constant-temperature type : AN1003 manufactured by AALab Systems. Each bridge is equipped with an amplifier and a home-made analogue filter (with a slope of −160 db/dec) in order to optimize the input to the A/D converter. This conversion was performed with a PCI-MIO-16-XE-10 board from National Instruments plugged in a PC. This board has a 16-bit resolution and a maximum data rate of 100 kHz. It is equipped with a sample-and-hold to ensure the simultaneity of the measurements with the X-wires. The data are stored on the PC hard disk and processed afterwards with our software.

The probes are mounted on DANTEC probe supports fixed on a wing-type profiled tube coming down from the ceiling of the tunnel. This tube is motorized in vertical translation and rotation in the horizontal plane. The accuracy is ± 0.01 mm and $\pm 0.01°$, respectively. This allows us to perform both the calibration of the probes at mid-height of the wind tunnel and the measurements in the BL without disconnection. No temperature correction is applied as the free-stream temperature differs by less than ± 0.2 K between calibration and measurements throughout the measurements. The free-stream velocity is regulated within ± 0.5 %. The distance from the probe to the wall is measured with a telescope with an accuracy of 0.05 mm.

The single-wire probes were calibrated using the usual King's law. The two coefficients and the exponent were obtained by a least-squares fitting on ten points distributed between 0.5 and 10 m s^{-1}. The X-wire probes were calibrated both in velocity and angle. Seven velocity values were used in the range 0.8–10 m s^{-1} and seven angles in the range ±12. A least-squares fit was performed on this data set with a generalized form of King's law. The calibration laws are used to convert the instantaneous voltages into instantaneous velocity components. The statistics are then computed on these discrete velocity signals.

The number of samples N_{acq} is related to the number of wires n, the sampling frequency F_{acq} and the record length T_{acq} by the relation: $N_{acq} = nT_{acq}F_{acq}$. The sampling frequency and the cutting frequency F_c of the filter were selected on the basis of an estimation of the Kolmogorov scales. The record length was selected by preliminary tests on the fourth-order moments. The convergence was considered completed when this moment was at less than 5 % of its fully converged value. This led to values of $T_{acq}U_e/\delta$ around 3000 in the viscous and buffer layer, 6000 in the log layer and 12 000 in the wake region (with a safety coefficient of 1.5). Table 1 gives

U_e (m s^{-1})	F_k (Hz)	F_c (Hz)	F_{acq} (Hz)	T_{acq} (s)	N_{acq} –
3	350	1000	2200	300	1 320 000
5	1000	2000	4200	180	1 512 000
7	2000	5000	11 000	120	2 640 000
10	4000	5000	11 000	90	2 090 000

TABLE 1. Acquisition parameters for $n=2$ et $T_{acq}U_e/\delta=3000$: U_e, free-stream velocity; F_k, Kolmogorov frequency; F_c, filter cutting frequency; F_{acq}, sampling frequency; T_{acq}, sample length; N_{acq}, number of samples.

U_e (m s^{-1})	$\epsilon_{rms}(\overline{u^1})$ (%)	$\epsilon_{rms}(\overline{u^2})$ (%)	$\epsilon_{rms}(\overline{u^4})$ (%)
3	1.20	4.71	9.40
5	0.71	3.45	6.57
7	0.68	3.51	6.48
10	0.74	2.77	5.50

TABLE 2. Root mean square error ϵ_{rms} at 95 % confidence for the four first moments of the longitudinal velocity fluctuation.

the value of the parameters used. T_{acq} and N_{acq} are given as example for the viscous and buffer layers.

As far as the accuracy is concerned, repeatability tests have been performed with the single-wire probe at $y^+=200$ and for the four free-stream velocities tested. From 50 successive measurements, the r.m.s. part of the error $\epsilon_{rms}(\overline{u^n})$ on the moment of order n can be estimated. The results are summarized in table 2 for a confidence level of 95 %.

These results are in fair agreement with those of Gilliot-Ottavy (1997) who used the same probes and calibration procedure for both single and X-wires. For X-wire probes, she came, after a detailed study, to an uncertainty estimation of, respectively, 1.3, 2.8 and 3.9 % for the first-, second- and fourth-order moments. The slightly higher values found here at 3 m s^{-1} are attributed to the fact that the wind-tunnel regulation is more sensitive at the lowest velocity and to the fact that the calibration is more difficult at very low velocities.

Bias should be negligible away from the wall if the calibration is properly done. When the probe is approaching the wall, there is a bias due to the aerodynamic interaction, the spurious heat transfer to the wall and, for X-wire probes, to the velocity gradient which becomes not negligible at the scale of the probe. No correction was applied for bias, the measurements were removed as soon as the mean velocity was visibly departing from the standard law.

2.3. *Boundary-layer statistical characteristics*

The main characteristics of the boundary layer are summarized in table 3. These were obtained from HWA experiments carried out at $x=19.6$ m, that is about 2 m downstream of the location of the PIV experiments. The wall shear stress was determined from the velocity profiles using the Clauser plot in the log region. The thickness parameters vary slowly with the external velocity. The pressure gradient remains very small while the friction velocity shows a nearly linear increase.

U_e (m s^{-1})	$P_{,x}$ (Pa m^{-1})	u_τ (m s^{-1})	ν/u_τ (μm)	δ (m)	δ^+ –	θ (m)	R_θ –	R_λ –
3	−0.057	0.110	136	0.345	2500	0.041	8100	300
5	−0.134	0.185	81	0.323	4000	0.035	11 500	400
7	−0.240	0.254	59	0.304	5100	0.032	14 800	460
10	−0.502	0.350	43	0.302	7000	0.031	20 600	570

TABLE 3. Turbulent boundary-layer characteristics: U_e, free stream velocity; $P_{,x}$, streamwise pressure gradient; u_τ, wall friction velocity; δ, BL thickness; θ, BL momentum thickness; R_θ, Reynolds number based on momentum thickness; R_λ, Reynolds number based on Taylor microscale.

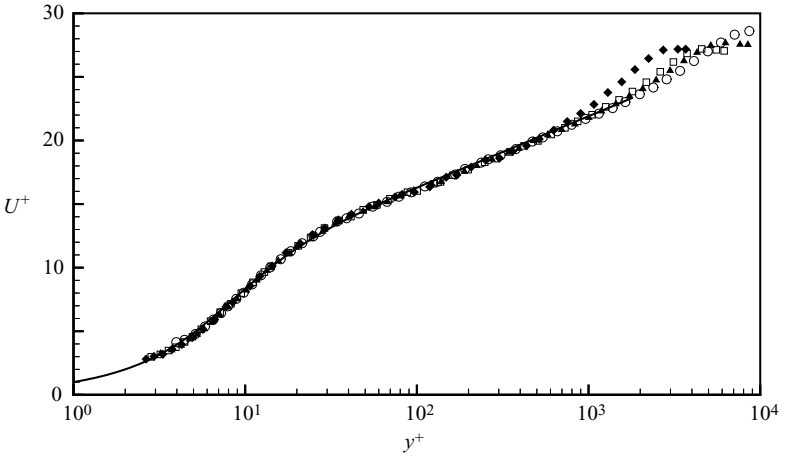

FIGURE 5. Profiles of longitudinal mean velocity U obtained with HWA: ◆, $R_\theta = 8100$; □, $R_\theta = 11\,500$; ▲, $R_\theta = 14\,800$; ○, $R_\theta = 20\,600$; ———, Van Driest profile.

The mean velocity profiles at the four Reynolds numbers are presented in figure 5, in the classical semi-logarithmic representation. These profiles show a good universality near the wall. They follow the classical Van Driest equation, (2.1), with the standard value of the von Kármán constant $\kappa = 0.41$. Thanks to the Reynolds-number range, they evidence a wide logarithmic region (one decade at least). The wake region is also clearly detectable and shows a classical shape and behaviour as a function of the Reynolds number. Although the Reynolds-number range covered is not so wide (about 3 times), even the lower value investigated does evidence a clear logarithmic region. This places the present data above the domain where low-Reynolds-number effects can be expected.

$$U^+(y^+) = \int_0^{y^+} \frac{2\,\mathrm{d}y^+}{b + \sqrt{b^2 + 4a\,(y^+)}} \quad \text{with} \quad \begin{cases} a(y^+) = [\kappa y^+(1 - \exp(y^+/c^+))]^2, \\ b = 1, \\ c^+ = 26. \end{cases} \tag{2.1}$$

Figure 6 shows the profiles of turbulence intensities for the four Reynolds numbers, scaled in wall units and as a function of both y/δ away from the wall and y^+ near the wall. A good universality is observed in both representations. In particular, the peak amplitude of all three fluctuations appear Reynolds-number independent in wall units. The slight departure of the X-wire measurements in the near-wall region at the largest

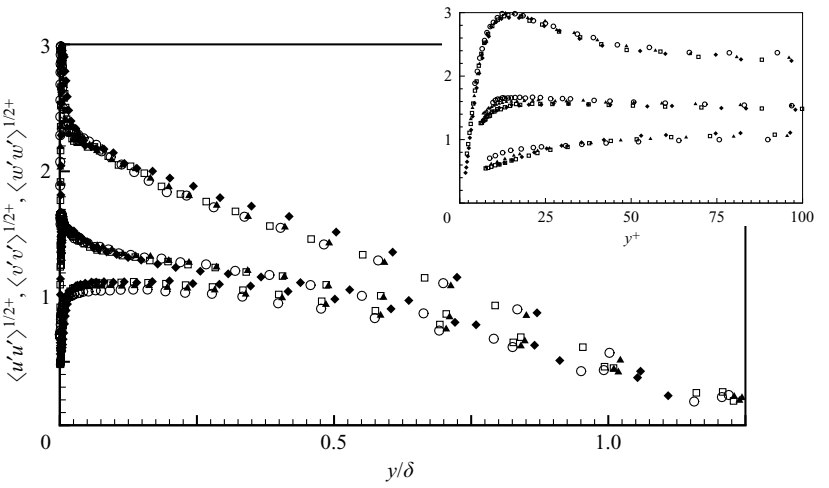

FIGURE 6. Profiles of turbulence intensities obtained with HWA: ◆, $R_\theta = 8100$; □, $R_\theta = 11\,500$; ▲, $R_\theta = 14\,800$; ○, $R_\theta = 20\,600$.

Reynolds number should be attributed to a probe-size effect. This point of the scaling of the peak amplitude of the streamwise velocity fluctuations has been addressed by several authors (DeGraaff & Eaton 2000; Marusic & Kungel 2003). The present measurements use hot wires of 2.5 μm in diameter by 500 μm in length. From table 3, the spatial resolution ranges from 0.02 to 0.06 in y^+ and 3.7 to 11.7 in z^+, which is comparable to DeGraaff & Eaton (2000). Besides, our acceleration parameter K is about 10 times smaller than theirs. A plot of the streamwise normal stress $\overline{u'^{2+}}$ (not shown here), shows that the value of the peak is in very good agreement with these authors at comparable Reynolds numbers. Moreover, the trend as a function of the Reynolds number is the same, but not as pronounced. DeGraaff & Eaton observe a variation of $\overline{u'^{2+}}$ between 7.7 and 9 for a variation of R_θ between 1430 and 13 000. Here, the variation is between 8.6 and 9.2 for R_θ between 8100 and 20 600. The Reynolds-number range covered in the present experiment is not enough, taking into account the measurement uncertainties, to decide between the wall scaling of the peak or the scaling proposed by DeGraaff & Eaton (2000) based on the skin friction coefficient C_f. A mean value of 0.32 of the peak in this representation is nevertheless in very good agreement in both experiments.

Figure 7 shows, in the same representation, the comparison of these turbulence intensities at $R_\theta = 8100$ with the measurements performed by Klebanoff (1955) at $R_\theta = 7500$ and Erm & Joubert (1991) at $R_\theta = 2788$, together with the DNS by Spalart (1988) at $R_\theta = 1410$. Although the peak of the longitudinal component is slightly higher than in the other studies, the overall agreement is fairly good. The y/δ representation clearly shows the Reynolds-number effect near the wall.

Figure 8 shows the profiles of the turbulent shear stress as a function of the Reynolds number. This quantity being much more sensitive, the universality in y/δ representation is less evident. A slight Reynolds-number effect is visible in this representation. Universality is better near the wall in wall units. The peak value is of the order of 0.8, which is attributed to a near-wall interaction effect.

To complete this characterization, figure 9 shows power spectra of u' at $R_\theta = 8100$ and for different wall distances and scaled with the wall distance. The inertial subrange clearly exist, at this Reynolds number, the results show that it extends when this

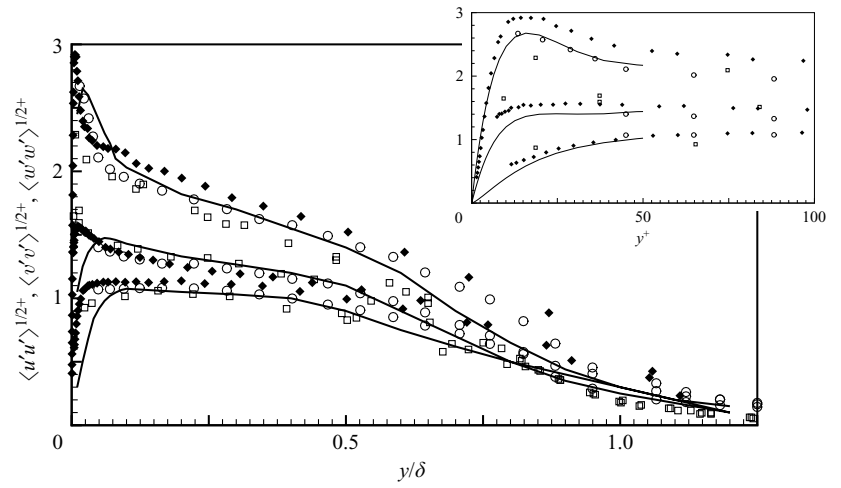

FIGURE 7. Profiles of turbulence intensities: ◆, present result at $R_\theta = 8100$; ○, Erm & Joubert (1991) at $R_\theta = 2788$; □, Klebanoff (1955) at $R_\theta = 7500$; ———, Spalart (1988) at $R_\theta = 1410$.

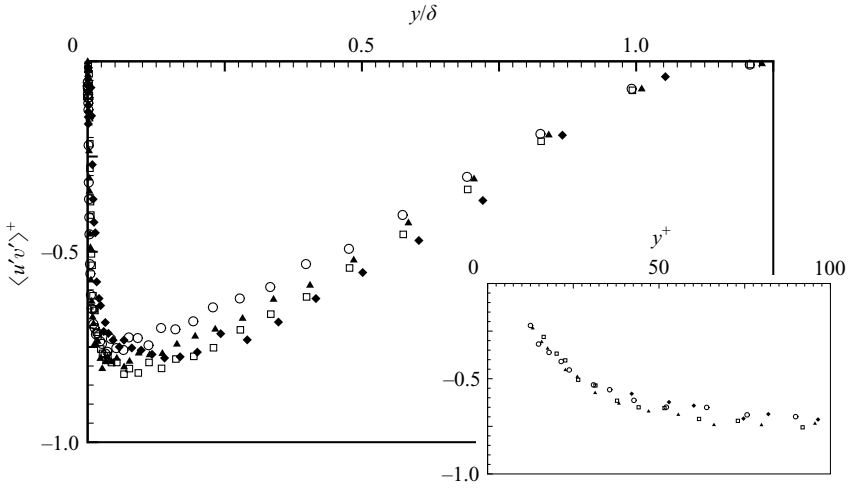

FIGURE 8. Profiles of turbulent shearing stress obtained with HWA: ◆, $R_\theta = 8100$; □, $R_\theta = 11\,500$; ▲, $R_\theta = 14\,800$; ○, $R_\theta = 20\,600$.

parameter increases. The horizontal part of the spectrum at high wavenumber gives an idea of the noise level. A region of -1 slope is also clearly visible from $y^+ = 25$ to 400, indicative of production of turbulence energy (Hinze 1975). This production range does not appear on the spectrum of the two other normal stresses (not shown here), in agreement with the Reynolds stress transport equations in a simple shear flow.

Much more results have been obtained from this hot-wire test campaign on the turbulence statistics. They will not be detailed here, as the results presented are enough to justify the standard characteristics of the boundary layer under study and as the main aim of the present contribution is to study turbulence organization. They will be discussed in further detail in a following paper.

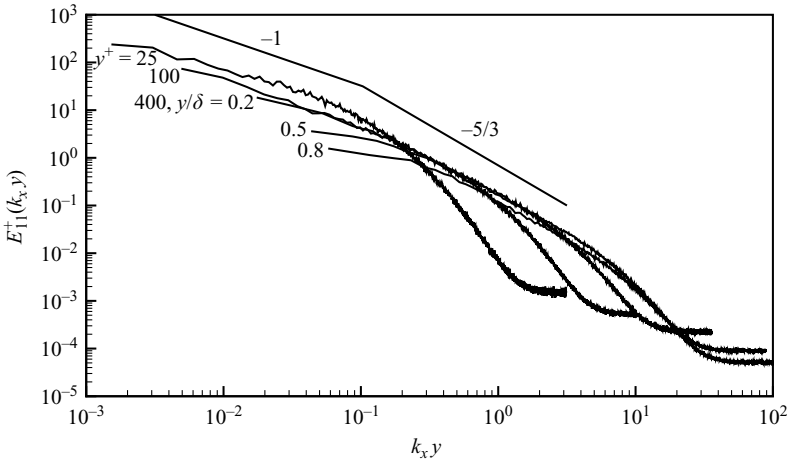

FIGURE 9. Power spectra of u' obtained with HWA at $R_\theta = 8100$.

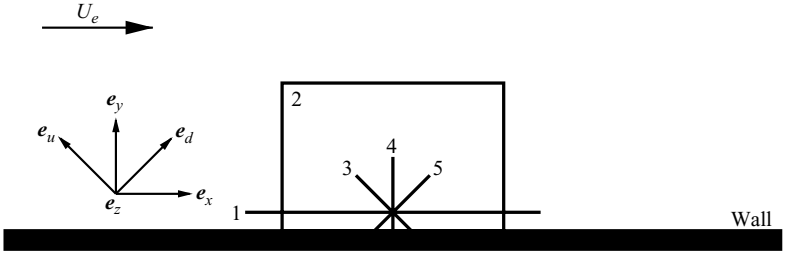

FIGURE 10. Orientations of the various planes used in the two series of PIV measurements: 1, (e_x, e_z); 2, (e_x, e_y); 3, (e_z, e_u); 4, (e_z, e_y); 5, (e_z, e_d).

3. PIV approach

As mentioned in § 1, the objective of this study is to use PIV to obtain quantitative information on the vortical structures encountered in the near-wall region of the boundary layer. To do so, the PIV experiments performed will be first described. Then, the PIV results will be validated statistically by comparison with the available HWA data. Finally, before presenting and discussing the results, the method used to extract the vortices from the PIV velocity maps will be detailed.

3.1. *PIV experiments performed*

We use two series of PIV measurements: 2D2C PIV by Carlier (2001) and 2D3C PIV by Kähler & Stanislas (2000) taken in the same facility. These measurements give access to two or three components of the instantaneous velocity maps in various planes. Figure 10 illustrates the orientations of the various planes used in the two series of PIV measurements. One unit vector has been defined to characterize each coordinate (e_x, e_y, e_z). Two additional vectors (e_u, e_d) are used to define simply the two tilted planes (upstream and downstream). The main characteristics of these measurements are summarized in table 4.

2D2C PIV measurements were carried out with a 2×330 mJ BMI ND-YAG laser and a Pulnix TM 9701 camera (484×768 pixels) in the planes (e_z, e_u) and (e_z, e_d) and with a Kodak DCS 460 camera (2048×3096 pixels) in the planes (e_x, e_y) and (e_x, e_z). The PIV records were analysed by a multigrid process with cross-correlation based

Plane configuration	$(\boldsymbol{e}_x, \boldsymbol{e}_y)$	$(\boldsymbol{e}_z, \boldsymbol{e}_y)$	$(\boldsymbol{e}_z, \boldsymbol{e}_u)$	$(\boldsymbol{e}_z, \boldsymbol{e}_d)$
PIV method	2D2C	2D3C	2D2C	2D2C
Field of view	$0.42^{\times} \times 0.28^{\times}$	$750^{+} \times 500^{+}$	$375^{+} \times 250^{+}$	$375^{+} \times 250^{+}$
Spatial resolution	$0.0017^{\times} \times 0.0017^{\times}$	$5.5^{+} \times 5.5^{+}$	$4.1^{+} \times 4.8^{+}$	$4.1^{+} \times 4.8^{+}$
Number of R_θ	4	1	4	4
Number of maps per R_θ	200	1565	800	800
Number of vectors per map	252×162	141×90	94×54	94×54

TABLE 4. PIV experiments characteristics.

on fast Fourier transform (FFT) and zero-padding. Two multigrid iterations were performed, respectively, with interrogation window sizes of 32×32 pixels and 16×16 pixels for the Pulnix camera and 64×64 pixels and 24×24 pixels for the Kodak camera. The correlation peaks were interpolated using three-point one-dimensional Gaussian peak fitting in two directions. In the planes $(\boldsymbol{e}_z, \boldsymbol{e}_u)$ and $(\boldsymbol{e}_z, \boldsymbol{e}_d)$, samples of 800 velocity maps were recorded for each of the four Reynolds numbers with a constant field size of $375^{+} \times 250^{+}$ in wall units. In the $(\boldsymbol{e}_x, \boldsymbol{e}_y)$ plane, samples of 200 velocity maps were recorded at the same Reynolds numbers with a constant field size of $0.42^{\times} \times 0.28^{\times}$ in external units. The general flow structure observed in the $(\boldsymbol{e}_x, \boldsymbol{e}_z)$-plane is not discussed in this paper. This has been studied extensively by Meinhart (1994), Meinhart & Adrian (1995), Zhou *et al.* (1999), Adrian *et al.* (2000*b*). After analysis by Carlier (2001) (and except for one point which will be discussed later), the results obtained here are in fair agreement with those of these authors as far as the flow structure is concerned. For this reason, only the statistics on the vortices will be presented in this plane. We will focus more on the other planes which have not yet been studied extensively with PIV.

2D3C PIV measurements were carried out with the same laser, but with two synchronized PCO cameras with a large CCD array (1024×1280 pixels). The opening angle between the two cameras in a stereo-imaging configuration with Scheimpflug correction was close to 86°. A second-order dewarping technique was applied for the evaluation of the stereoscopic images. The interrogation of the data was performed with the FFT-based free shape cross-correlation. The interrogation window size was 32×32 pixels. A two-dimensional Gaussian fit using the Levenberg–Marquardt method was applied to find the correlation peak position. A total of 1565 velocity maps at $R_\theta = 7500$ were obtained in the $(\boldsymbol{e}_z, \boldsymbol{e}_y)$-plane with a field size of $750^{+} \times 500^{+}$. In both experiments, the time interval was chosen to have displacements around 10 px.

3.2. *PIV validation*

Particle image velocimetry is a fairly recent measurement technique, especially in its digital form. The theory has been thoroughly developed (see Keane & Adrian 1992; Westerweel 1997) and is still an active subject of research, but the application to turbulence with large data sets has been limited up to now. It is thus of interest, having here fairly large numbers of realizations, to compare the statistics from PIV to those of HWA. To enhance the convergence, the averaging has been performed when possible along x and z, supposing the homogeneity of the flow along x at the scale of the PIV field of view.

Figure 11 presents the mean velocity profiles measured in the $(\boldsymbol{e}_x, \boldsymbol{e}_y)$-plane at $R_\theta = 7500$ and 19 000 and in the $(\boldsymbol{e}_z, \boldsymbol{e}_y)$ at $R_\theta = 7500$ and 13 500. Here again, the wall shear stress was deduced from the Clauser plot of the data in the log layer. The accuracy on the wall shear stress with this method is of the order of 5 %. As good

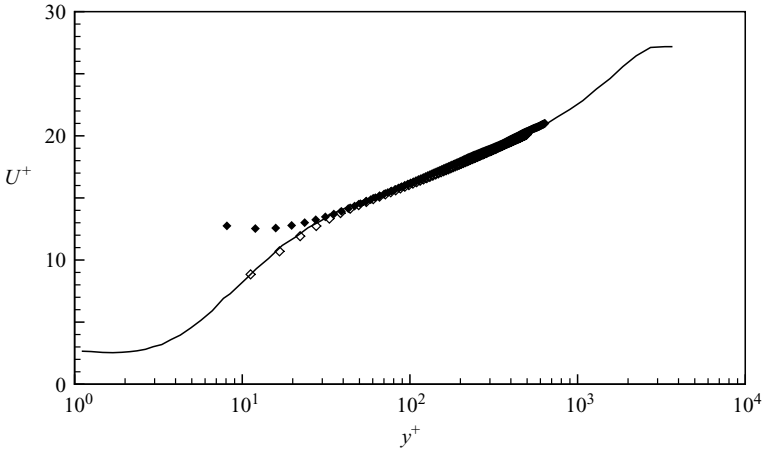

FIGURE 11. Profiles of longitudinal mean velocity U: ———, HWA at $R_\theta = 8100$; ◆, PIV at $R_\theta = 7500$ in $(\boldsymbol{e}_x, \boldsymbol{e}_y)$-plane; ◇, PIV at $R_\theta = 7500$ in $(\boldsymbol{e}_z, \boldsymbol{e}_y)$-plane; ○, PIV at $R_\theta = 19\,000$ in $(\boldsymbol{e}_x, \boldsymbol{e}_y)$-plane.

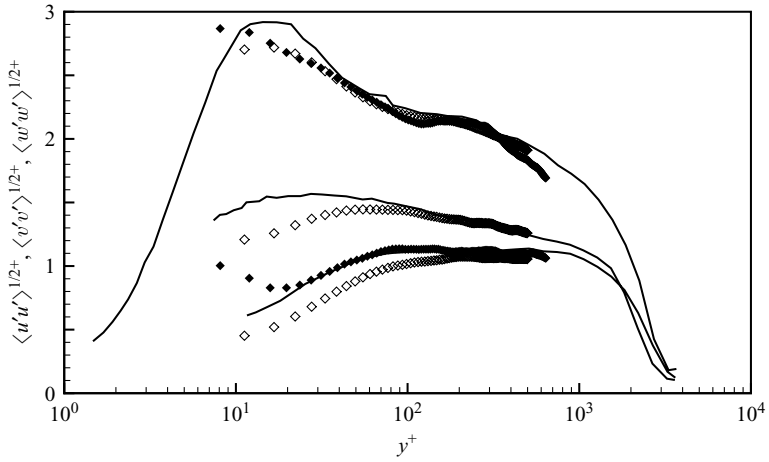

FIGURE 12. Profiles of turbulence intensities: ———, HWA at $R_\theta = 8100$; ◆, PIV at $R_\theta = 7500$; ▲, PIV at $R_\theta = 13\,500$.

universality was shown from the hot-wire data, these profiles are compared to HWA at $R_\theta = 8100$ only. At the lowest Reynolds number, the agreement is very good in the log layer for both planes, while a bias appears in the buffer layer for the $(\boldsymbol{e}_x, \boldsymbol{e}_y)$-plane. This is a well-known phenomenon and is due to the velocity gradient being not negligible at the scale of the PIV interrogation window in the $(\boldsymbol{e}_x, \boldsymbol{e}_y)$-plane (see Meinhart 1994). This is confirmed by the fact that this bias does not appear in the $(\boldsymbol{e}_x, \boldsymbol{e}_z)$-plane where the main gradient is through the plane. Such a bias can now be reduced by using a PIV algorithm with interrogation window deformation (see Scarano 2002) which was not available at the time of the experiments. At $R_\theta = 19\,000$, the gradient bias affects slightly the data in the $(\boldsymbol{e}_x, \boldsymbol{e}_y)$-plane under $y^+ = 100$. In fact, this bias on the mean velocity will not affect the results presented here as they are based on the fluctuating part of the velocity vector. Away from the wall, the profile shape shows that the wake region is not covered by the PIV data, owing to the limited field of view.

The turbulence intensities measured in the same two planes are compared to HWA data in figure 12 for $R_\theta = 7500$ and 13 500 where all three components are available.

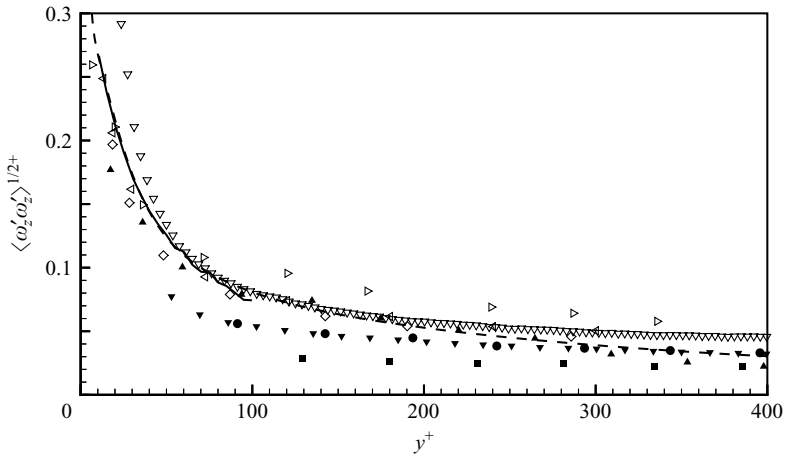

FIGURE 13. Profiles of r.m.s. spanwise vorticity ω_z' scaled in wall units: ▽, PIV at $R_\theta = 7500$; ▼, PIV at $R_\theta = 13\,500$; ▲, Adrian *et al.* (2000*b*) $R_\theta = 930$; ●, Adrian *et al.* (2000*b*) $R_\theta = 2370$; ■, Adrian (2000*b*) $R_\theta = 6845$; ▷, Klewicki & Falco (1990) $R_\theta = 1010$; ◁, Klewicki & Falco (1990) $R_\theta = 2870$; ◇, Klewicki & Falco (1990) $R_\theta = 4850$; ———, Spalart (1988) $R_\theta = 670$; - - -, Del Alamo & Jimenez (2003) $Re_\tau = 550$.

Apart for the v' component in the $(\boldsymbol{e}_z, \boldsymbol{e}_y)$-plane which is slightly underestimated at $R_\theta = 7500$, the agreement is fairly good between the two planes and with the hot-wire data, indicating that the bias on the mean velocity observed in figure 11 does not affect the fluctuating components so much.

As the characteristics of vortical structures will be looked at in detail in the present contribution, it is of interest to look at the statistical properties of the vorticity in the region of interest. For that purpose, the instantaneous vorticity was computed from the PIV velocity maps, using a second-order centred difference scheme. This vorticity was averaged over the ensemble of the maps and the directions of homogeneity (x or z, depending on the recording plane) to compute the mean profile along y. Then the r.m.s. profile of the corresponding vorticity component was computed by subtracting this mean profile. Figure 13 shows the comparison of the profile obtained for the spanwise component ω_z' at $R_\theta = 7500$ and 13 500 with the data of Adrian *et al.* (2000*b*), Klewicki & Falco (1990), Spalart (1988) and Del Alamo & Jimenez (2003) for $y^+ < 400$. The representation is in wall units. Very near the wall ($y^+ < 30$), the PIV noise is expected to enhance artificially the r.m.s. of the vorticity (as a derivative quantity). The global agreement with the existing data is fairly good. Even the effect of the Reynolds number, that is a decreasing level with increasing Reynolds number, is coherent with the findings of others (Adrian *et al.* 2000; Klewicki & Falco 1990), although the levels are different between the different studies. This is probably due to the difficulty of measuring this quantity very accurately with any technique.

Figure 14 gives the spanwise and streamwise r.m.s. components of ω' for $y^+ < 100$ compared to the data of Spalart (1988), Ong & Wallace (1998) and Del Alamo & Jimenez (2003). For Ong & Wallace (1998), the data scaled with both u_τ (deduced from the Clauser plot) and u_* (estimated) are given. The present results compare favourably with both the DNS and the experimental data. For ω_z', the stronger increase very near the wall of the present data should be attributed to the noise increase on derivatives in this region. The ω_x' shows here a peak around $y^+ = 25$. Such a peak is detectable on both DNS data too, but it is smoother and nearer to the wall

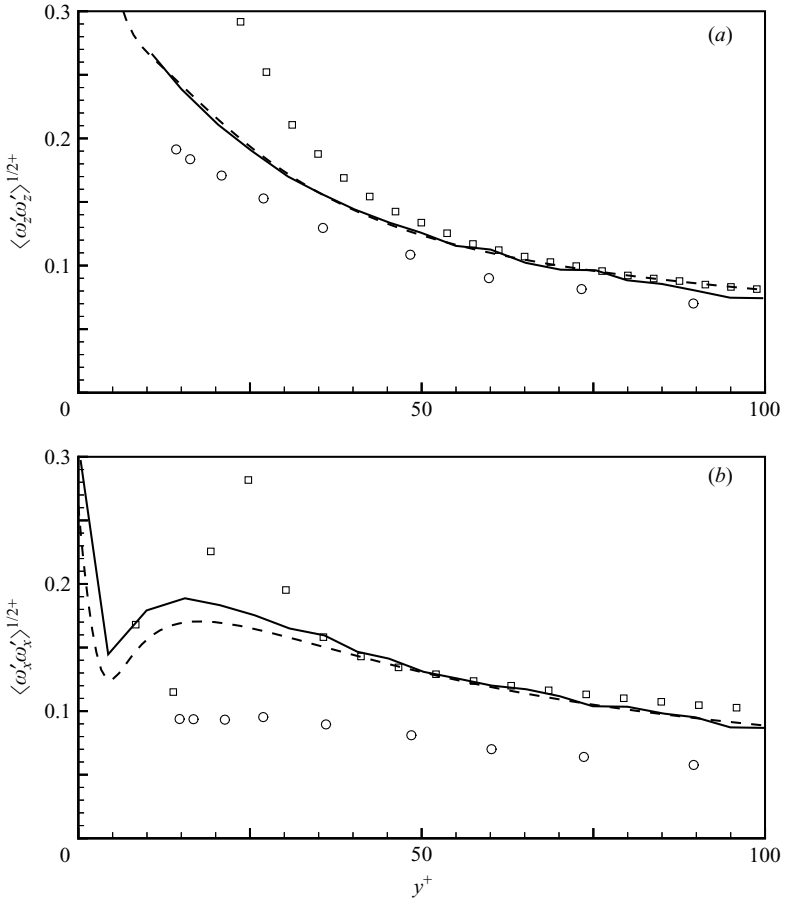

FIGURE 14. Profiles of r.m.s. (*a*) spanwise vorticity ω_z' and (*b*) streamwise vorticity ω_x'): □, present PIV at $R_\theta = 7500$; ○, Ong & Wallace (1998) $R_\theta = 4850$; ——, Spalart (1988) $R_\theta = 670$; - - - , Del Alamo & Jimenez (2003) $Re_\tau = 550$.

($y^+ = 15$). The difference in amplitude of this peak is questionable. It is clear that, in this very near wall region, it may be emphasized by PIV errors. Nevertheless, as will be seen later, this $y^+ = 25$ location is important as far as the vortex generation process is concerned.

Figure 15 shows the probability density function of u' computed from the PIV experiments at $y^+ = 100$ and $R_\theta = 7500$ in the planes $(\boldsymbol{e}_x, \boldsymbol{e}_y)$ and $(\boldsymbol{e}_z, \boldsymbol{e}_y)$. The same quantity from HWA experiments is also shown at $y^+ = 100$ and $R_\theta = 8100$. In the $(\boldsymbol{e}_x, \boldsymbol{e}_y)$-plane, a regular oscillation appears around the HWA result. The oscillation period corresponds to a length of 1 pixel in the image plane. It is due to the 'peak-locking effect', which skews the evaluated displacement of particle images towards integer values of pixels. This is true also in the two tilted planes. This peak-locking does not appear in the $(\boldsymbol{e}_z, \boldsymbol{e}_y)$-plane, owing to the use of a more sophisticated peak-fitting algorithm, but also to the stereoscopic reconstruction algorithm which smoothes this random bias. Sub-pixel local shift, as proposed by Lecordier (1997), decreases this peak-locking effect. However, this technique was not available at the time of the analysis and it has been demonstrated since then that this peak-locking behaves as a high-frequency random noise (see Foucaut & Stanislas 2002). This will

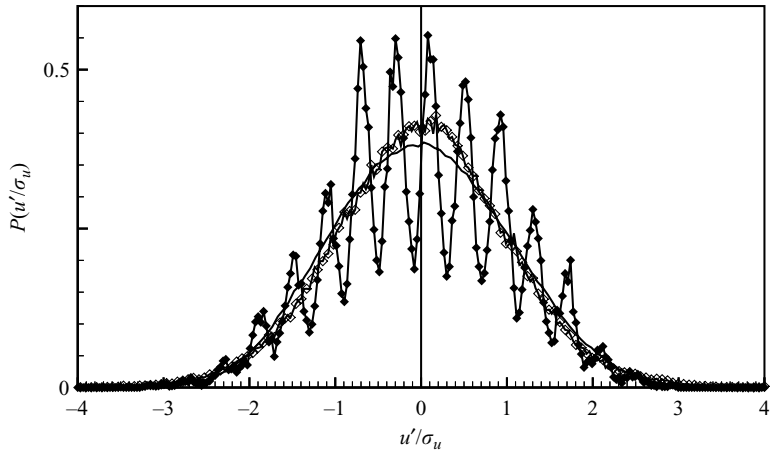

FIGURE 15. Probability density function of u' at $y^+ = 100$: ———, HWA at $R_\theta = 8100$; ◆, PIV at $R_\theta = 7500$ in $(\boldsymbol{e}_x, \boldsymbol{e}_y)$-plane; ◇, PIV at $R_\theta = 7500$ in $(\boldsymbol{e}_z, \boldsymbol{e}_y)$-plane.

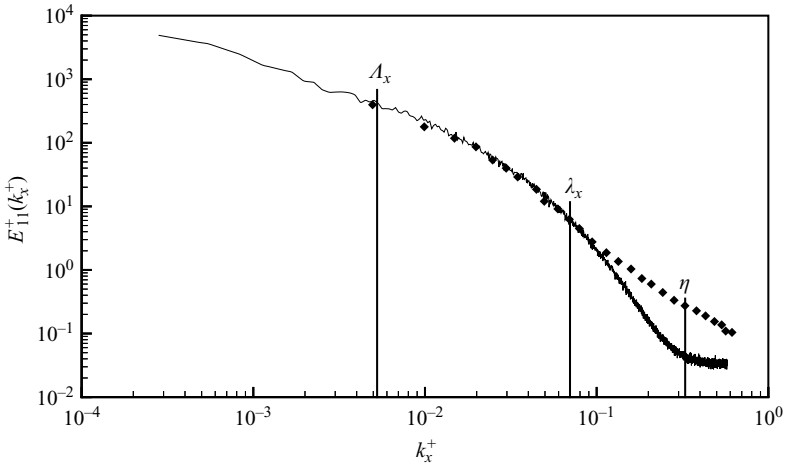

FIGURE 16. Power spectra of u' at $y^+ = 100$: ———, HWA at $R_\theta = 8100$; ◆, PIV at $R_\theta = 7500$ in $(\boldsymbol{e}_x, \boldsymbol{e}_y)$-plane.

be confirmed later in this paper by the coherence of the results in the different planes. It is also supported by the fact that the number of oscillations inside the PDF is large enough not to affect the covariance tensor estimation (see Carlier 2001).

Using the same data, figure 16 shows the power spectra of u' obtained with PIV and HWA (thanks to the 'Taylor hypothesis'). k_x is the spatial wavenumber. The common part covers about one decade. This range contains the Taylor microscales λ and integral scales Λ, but not the Kolmogorov scales η. Improvement towards the small scales depends on the reduction of PIV noise which has been characterized by Foucaut, Carlier & Stanislas (2000). Extension towards the large scales depends solely on the field of view. Note that the range of available scales is essentially linked to the number of pixels on the CCD sensor on the low-wavenumber side and to the noise level toward the high wavenumbers. This is due to the specificity of the turbulence signal: the energy decreases with increasing wavenumber. It should also be noted

that the range of structures of interest in the present study, which is above the Taylor microscale, is not affected by the PIV noise.

3.3. *Eddy structure detection method*

It is difficult to define an eddy structure. Robinson (1991) proposed the following definition: 'a vortex exists when instantaneous streamlines mapped onto a plane normal to the vortex core exhibit a roughly circular or spiral pattern, when viewed from a reference frame moving with the centre of the vortex core'. One difficulty, which has been addressed by several authors (Jeong & Hussain 1995; Adrian *et al.* 2000*a*), is to find a reliable quantitative criterion corresponding to this definition. The vorticity alone is not reliable enough, as there is a significant amount of vorticity in a shear layer. The problem is thus to distinguish between a 'vortex' and a local shear layer. In practice, it is impossible to detect all the vortices, especially from experimental data. In fact, it is not necessary to do so. It is necessary only to make sure that the detected population is large enough to obtain converged statistics and that it is fully representative of the population under study (that is, no bias is introduced by a criterion missing a specific part of the population).

Jeong & Hussain (1995) concluded that 'instantaneous vorticity fields are inadequate to reveal coherent structures in turbulent boundary layers'. They reviewed several mathematical criteria to detect vortices in numerical simulations: maximum value of vorticity magnitude $\|\boldsymbol{\omega}\|$; maximum value of the second invariant Q of the velocity gradient tensor; maximum value of the discriminant Δ; maximum of the complex eigenvalue λ_2 of the velocity gradient tensor. They came to the conclusion that this last criterion is the most efficient one. As an example, Christensen & Adrian (2002) have detected the eddy structures in PIV velocity maps using the swirling strength (which corresponds in two dimensions to this λ_2 criterion). However, the spatial coherence concept is not considered in these formalisms. Wavelet transforms can overcome this problem (see Bonnet *et al.* 1998; Schram & Riethmuller 2000). Indeed, this mathematical tool is connected, like pattern recognition, to the convolution product between a signal and a model, called a mother wavelet, but as a function of the scale. It can be applied, for example, to the enstrophy field or more generally to scalar fields from the various criteria reviewed by Jeong & Hussain (1995).

Nevertheless, because of their derivative nature, it is difficult to estimate these criteria with a low noise level from PIV experiments, especially based on autocorrelation images (see Foucaut *et al.* 2000) without applying some kind of low-pass filtering. This is why a simple pattern recognition analysis based on the convolution product was preferred for identifying parts of the velocity maps similar to a model which defines a reference eddy structure (see Scarano, Benocci & Riethmuller 1999). This procedure is applied in order to obtain the main characteristics of the eddy structures by building the indicative functions of their location within the velocity maps.

The selected eddy structure model is, in polar coordinates, a tangential velocity component with Gaussian damping:

$$\boldsymbol{u}(r,\theta) = \exp -\left(\frac{r}{\sigma}\right)^2 \cdot \boldsymbol{e}_\theta, \tag{3.1}$$

where $\boldsymbol{e}_\theta$ is the tangential unit vector in polar coordinates. The Gaussian damping limits the influence of the surrounding flow far from the core by using a damping radius σ. Such a model allows us to filter local shear layers which contain vorticity, but does not fit the definition of Robinson. The model and the velocity map are

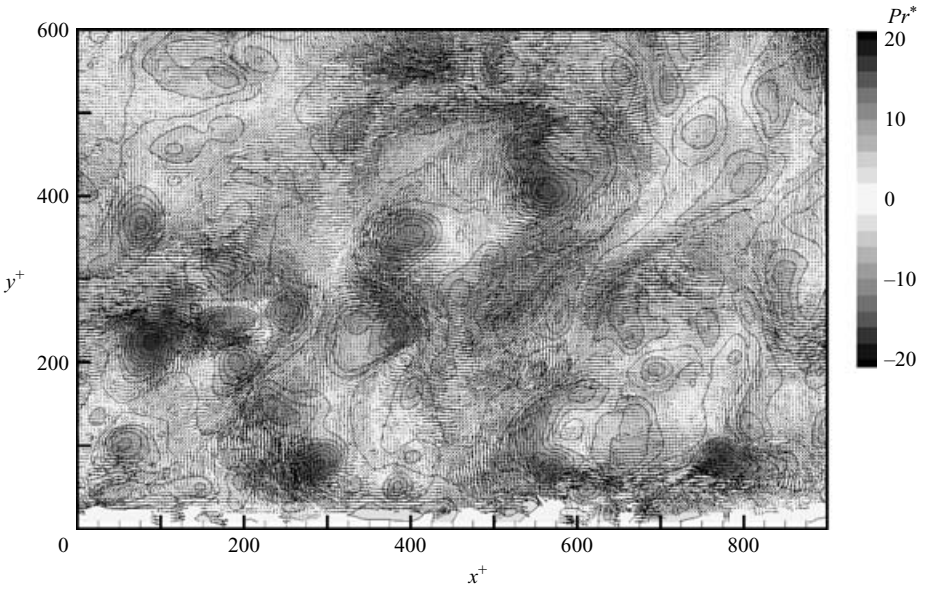

FIGURE 17. Sample of instantaneous velocity map in the $(\boldsymbol{e}_x, \boldsymbol{e}_y)$-plane at $R_\theta = 7500$. The mean velocity profile has been substracted. Contours of the detection function Pr^* are shown in the background to highlight eddy structure locations.

projected onto $\boldsymbol{e}_\alpha$. Both resulting scalar maps are convolved together to give R_α which depends on α:

$$R_\alpha = (\boldsymbol{u}_{model} \cdot \boldsymbol{e}_\alpha) \otimes (\boldsymbol{u}_{map} \cdot \boldsymbol{e}_\alpha). \tag{3.2}$$

The mean value $\overline{R}$ and the variance R' are defined by the following equations:

$$\overline{R} = \langle R \rangle_\alpha, \tag{3.3}$$

$$R' = \sqrt{\langle R_\alpha - \overline{R} \rangle_\alpha^2}, \tag{3.4}$$

where $\langle \cdots \rangle_\alpha$ is the statistical averaging operator along α. A location of high $\overline{R}$ indicates a high similarity level between the model and the velocity map. A location of low R' indicates an isotropic shape of the velocity map. The combination of both parameters allow us to build a detection function which will favour the detection of effective eddy structures (having a 'relatively' isotropic shape) rather than simple shear layers (which generally have a strong anisotropic shape, but a strong vorticity). This detection function is defined as:

$$Pr^* = \frac{\overline{R}}{1 + (R'/\overline{R})^2}. \tag{3.5}$$

Peaks appearing in the detection function indicate probable positions of eddy structures in the velocity map. Figure 17 gives an example of an instantaneous velocity map in the $(\boldsymbol{e}_x, \boldsymbol{e}_y)$-plane with the corresponding contours of the detection function. At this stage, the function used can be compared to the derivative-based criteria by Jeong & Hussain (1995) mentioned above. Such a comparison is done further downstream.

As illustrated by figure 17, the detection function shows clear peaks at the locations of vortices but, of course, also some more or less strong peaks at other flow features.

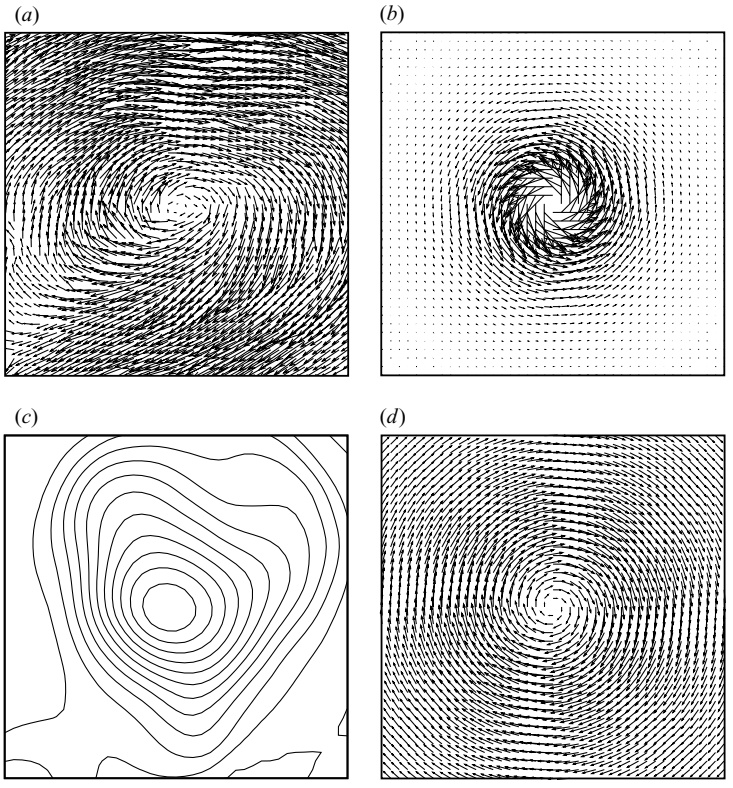

FIGURE 18. (*a*) Sub-region of the fluctuating velocity field containing an eddy structure, (*b*) eddy structure model, (*c*) detection function and (*d*) nearest Oseen vortex.

In order to avoid defining directly a threshold on the detection function, with the risk either of filtering out a number of vortices or of accepting objects which are not vortices, it was decided to add a second step to the detection procedure. In this second step, all the regions around peaks of the detection function above a fairly low threshold are fitted with an Oseen vortex model (see equation (3.6)) by a least-squares procedure (Levenberg–Marquardt method).

$$\boldsymbol{u}(r,\theta) - \boldsymbol{u}_o(\boldsymbol{x}_o) = \frac{\Gamma_o}{2\pi}\frac{1}{r}\left[1 - \exp -\left(\frac{r}{r_o}\right)^2\right] \cdot \boldsymbol{e}_\theta \tag{3.6}$$

with $\boldsymbol{r} = \boldsymbol{x} - \boldsymbol{x}_o$.

The vortex parameters fitted are the coordinates of the centre $\boldsymbol{x}_o$, the convection velocity $\boldsymbol{u}_o$, the circulation Γ_o and the radius r_o. The vorticity at the centre is $\omega_o = \Gamma_o/(\pi r_o^2)$ (with $\boldsymbol{\omega} = \vec{\text{rot}}\,\boldsymbol{u}$). The same Gaussian damping as for the detection was used in the least-squares fit for the same reason. If the regression coefficient (similarity level) is larger than a selected threshold T, the corresponding eddy structure candidate is retained and the parameters obtained characterize it. The first interest of this approach is to select, among all the detected objects, those which look like a vortex, depending, of course, on the value given to the two adjustable parameters of the model: the threshold T and the radius σ. The second interest is to provide both a length scale r_o and a vorticity scale ω_o characteristic of the vortex.

Figure 18 presents different steps of the eddy structure identification method. It clearly shows in this case that the real vortex is not circular, but more elliptic. The

Threshold T	0.925	0.925	0.925	0.900	0.950
Damping radius σ^+	39	31	23	23	23
Mean radius $\langle r_o \rangle^+$	27	25	22	22	23
Mean vorticity $\langle \omega_o \rangle^+$	−0.164	−0.172	−0.180	−0.176	−0.200
Number of eddy structures	2363	2787	2672	3309	1394

TABLE 5. Sensitivity of the eddy structure identification method (checked in the $(\boldsymbol{e}_x, \boldsymbol{e}_y)$-plane at $R_\theta = 7500$).

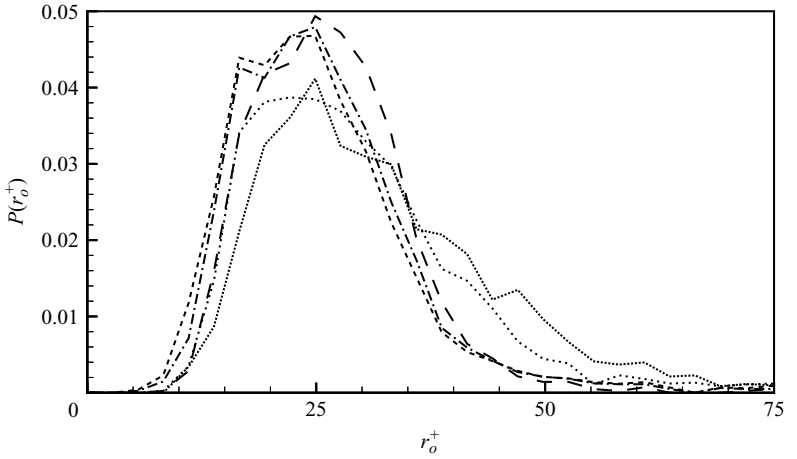

FIGURE 19. Probability density function of r_o in the $(\boldsymbol{e}_x, \boldsymbol{e}_y)$ plane at $R_\theta = 7500$: . . . , $T = 0.925$, $\sigma^+ = 39$; ···, $T = 0.925$, $\sigma^+ = 31$; −·−, $T = 0.925$, $\sigma^+ = 23$; - - -, $T = 0.900$, $\sigma^+ = 23$; − − −, $T = 0.950$, $\sigma^+ = 23$.

parameters determined with the least-squares fitting of the Oseen model are the 'nearest isotropic estimation'. For more detail, one should at least introduce two length scales and one angle for the two main axes of the ellipse, instead of a simple radius for a circle. More details on the present method are given by Carlier (2001).

Before applying the described detection method, the sensitivity of the results to T and σ has to be characterized and suitable values of both parameters have to be chosen. Table 5 gives the mean radius $\langle r_o \rangle$ ($\langle \cdots \rangle$ is the ensemble averaging operator), the mean vorticity $\langle \omega_o \rangle$ and the number of eddy structures detected in the $(\boldsymbol{e}_x, \boldsymbol{e}_y)$-plane at $R_\theta = 7500$ for different values of T and σ. Increasing T decreases strongly the number of eddy structures detected and increases slightly the mean vorticity $\langle \omega_o \rangle$. The mean radius $\langle r_o \rangle$ is not sensitive to this parameter. Generally, opposite to the particular case shown in table 5, increasing σ decreases slightly the number of eddy structures detected because the smallest eddies are filtered out. Here, the mean radius $\langle r_o \rangle$ increases, but much more slowly than σ. The mean vorticity $\langle \omega_o \rangle$ decreases, but only slightly.

Figures 19 and 20 present, respectively, the normalized probability density function of r_o and ω_o in the $(\boldsymbol{e}_x, \boldsymbol{e}_y)$-plane at $R_\theta = 7500$ using the same detection parameters as in table 5. The effect of σ is more visible. The trends can be explained by the fact that the detection method behaves like a band-pass filter which moves toward large radius when σ increases. The minimum damping radius σ of 23^+ (equivalent to 6 grid spacings at $R_\theta = 7500$) seemed to allow the detection of eddy structures from

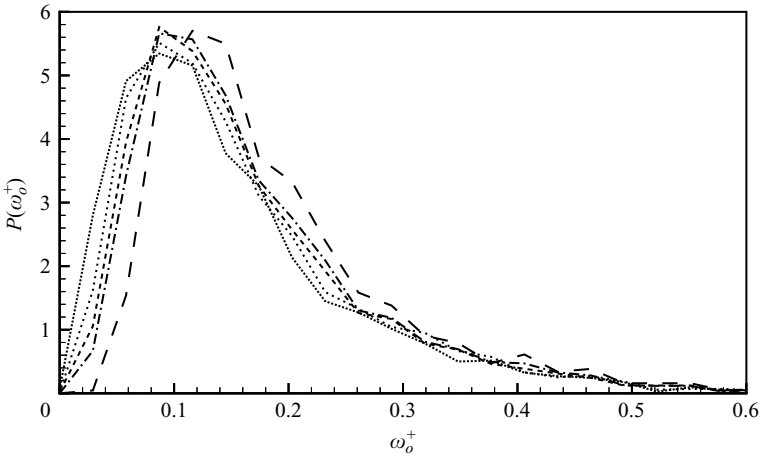

FIGURE 20. Probability density function of ω_o in the $(\boldsymbol{e}_x, \boldsymbol{e}_y)$-plane at $R_\theta = 7500$: ..., $T = 0.925$, $\sigma^+ = 39$; $\cdots$, $T = 0.925$, $\sigma^+ = 31$; $-\cdot-$, $T = 0.925$, $\sigma^+ = 23$; - - -, $T = 0.900$, $\sigma^+ = 23$; $--$, $T = 0.950$, $\sigma^+ = 23$.

the smallest one resolved by the velocity maps (around 15^+ in the present case) up to vortices of about half the PIV field size. Besides, figures 19 and 20 give a good indication of the non-Gaussian distribution of the characteristics of the structure around the mean values which will be described and discussed in § 4. The individual analysis of the detection results shows that the use of a threshold T of 0.925 is the best compromise for selecting a maximum number of real eddy structures with a minimum number of mistakes.

In order to compare the present indicative function to other now standard methods, one sample was selected in the $(\boldsymbol{e}_z, \boldsymbol{e}_y)$-plane. Figure 21($a$) gives the instantaneous velocity map of this sample. The interest of this plane is two-fold: (i) the images are of cross-correlation type (that is less noisy); (ii) the mean velocity is through the plane so that no mean convection velocity has to be substracted. Figures 21(b), 21(c) and 21(d) show, respectively, the streamwise vorticity ω_x, the reduced discriminant Dr (which is equivalent in two dimensions to the swirling strength) and the present indicative function named Pr. The two indicative functions based on derivatives had to be smoothed with a 5×5 sliding average. The absolute value of ω_x and Pr were used, as the sign of the vortex is not relevant for the present comparison. Each function has been scaled to its maximum value in the map. The circles indicate the location of the vortices which have been obtained by applying the Oseen fit to each of these three indicative functions. The parameters for the Oseen fit were the same for the three functions and the same as that used to obtain the following results. First of all, the comparison of figure 21(b) with the others clearly illustrates the arguments on vorticity as an indicative function discussed above. A second point which appears clearly is that the present indicative function Pr gives smoother and broader peaks than the reduced discriminant. Looking at the retained vortices, 24 are obtained with ω_x, 24 with Dr and 27 with Pr. Among those, three are wrong with ω_x (the two on the upper right-hand border and one at $y^+ = 300$, $z^+ = 100$). None are wrong with the two other criteria, which means that Dr is missing 6 vortices while Pr is missing 3 of them in a total population of 30 vortices in this map. For the common vortices,

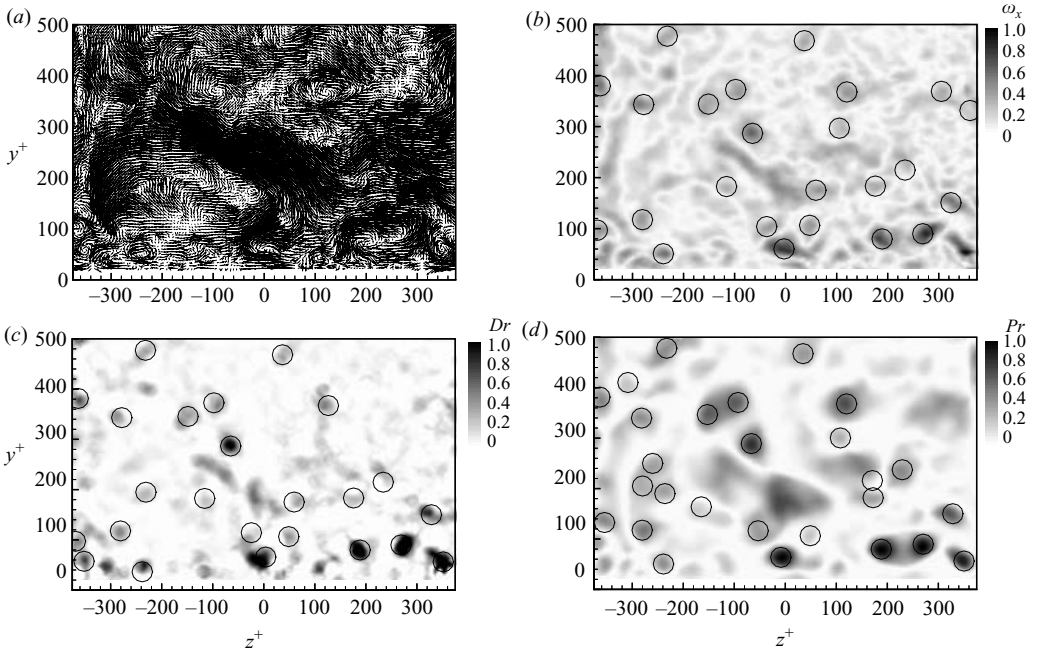

FIGURE 21. Comparison between different detection functions computed from one sample of intantaneous PIV velocity map. (*a*) Sample of instantaneous velocity field in the $(\boldsymbol{e}_z, \boldsymbol{e}_y)$-plane, (*b*) vorticity component normal to the plane $|\omega_x|$, (*c*) reduced discriminant Dr; (*d*) present indicative function $|Pr|$. The circles indicate the local extrema of each function where the Oseen vortex-fitting algorithm indicates the presence of a vortex.

the agreement on the size and vorticity given by the Oseen fit is very good between the three indicative functions.

Figure 22 gives some representative examples of accepted eddy structures in the $(\boldsymbol{e}_z, \boldsymbol{e}_u)$-plane at $R_\theta = 7500$, while figure 23 shows examples of rejected eddy structures. The detected (or rejected) vortices are centred at the crossing of the horizontal and vertical lines in each map. As can be seen, all the detected objects are clearly vortical structures which sometimes are far from being isotropic, but are in good coherence with their direct environment. As shown by figure 23, some vortices are also rejected. It appears that they are generally weaker vortices in an active environment and with a lower coherence with this environment (apart for the upper right-hand one). Consequently, the detector appears to segregate more or less between 'active' and 'inactive' vortices. We can thus expect the selected population to be statistically representative of 'active' vortices as defined by Robinson. A few of these structures go through the detector, but they do not show a specific character. Thus, only the results on the number of vortices must be looked at with some care, as they are based on the hypothesis that the same proportion of the 'active' vortices population is detected in all planes and at all Reynolds numbers.

4. PIV results

The results presented in this section come from PIV experiments carried out in the planes $(\boldsymbol{e}_z, \boldsymbol{e}_u)$, $(\boldsymbol{e}_z, \boldsymbol{e}_y)$ and $(\boldsymbol{e}_z, \boldsymbol{e}_d)$. As turbulence is homogeneous in the transverse direction, the averaged results from eddy structures having opposite vorticity are the

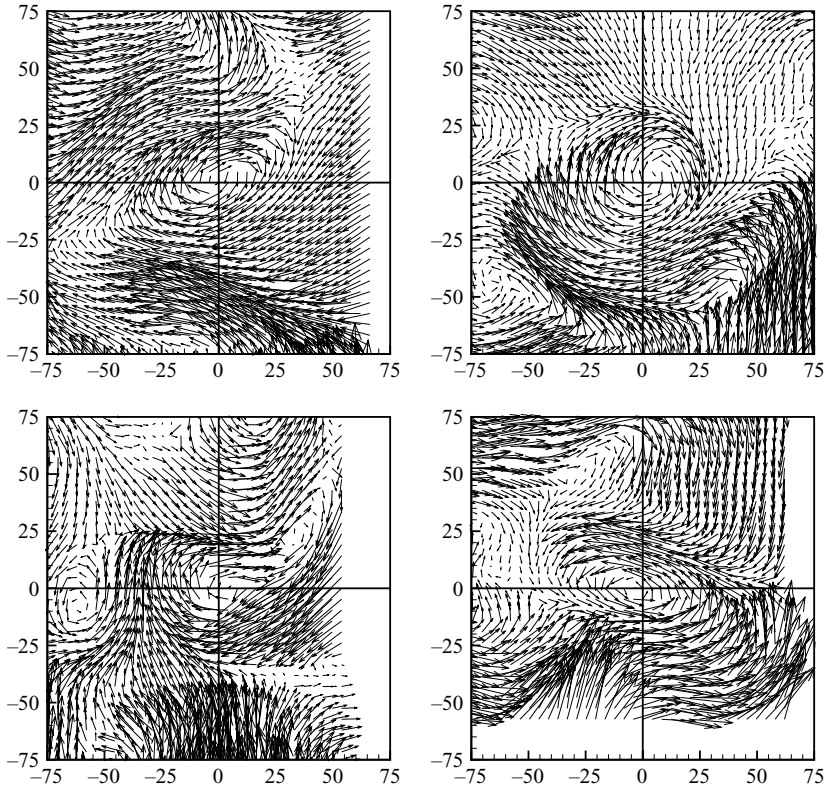

FIGURE 22. Examples of accepted eddy structures in the $(\boldsymbol{e}_z, \boldsymbol{e}_u)$-plane at $R_\theta = 7500$.

	$(\boldsymbol{e}_x, \boldsymbol{e}_y)$		$(\boldsymbol{e}_z, \boldsymbol{e}_u)$		$(\boldsymbol{e}_z, \boldsymbol{e}_y)$		$(\boldsymbol{e}_z, \boldsymbol{e}_d)$	
R_θ	V_-	V_+	V_-	V_+	V_-	V_+	V_-	V_+
7500	3613	1726	2386	2393	10 979	10 871	800	822
10 500	–	–	2096	2123	–	–	586	639
13 500	–	–	2423	2408	–	–	852	832
19 000	–	–	2303	2342	–	–	756	769

TABLE 6. Number of eddy structures detected.

same for each of these three planes. This was checked first and results of both types could then be averaged together in order to improve the convergence. These results are, for the different orientations of the plane and at different Reynolds numbers : the averaged eddy structure velocity map; the number of eddy structures detected; the mean radius; the mean vorticity at the centre; and the spatial relationships with other coherent structures. Table 6 summarizes the number of eddy structures used for the assessment of these results. For convergence reasons, the standard deviations were not computed as a function of the wall distance. However, figures 19 and 20 give a good idea of the distributions.

In figure 17, the grey levels represent the detection function of the eddy structures in the $(\boldsymbol{e}_x, \boldsymbol{e}_y)$-plane. As mentioned earlier, as this plane has been studied extensively by Adrian and colleagues, the present results in this plane will not be further discussed

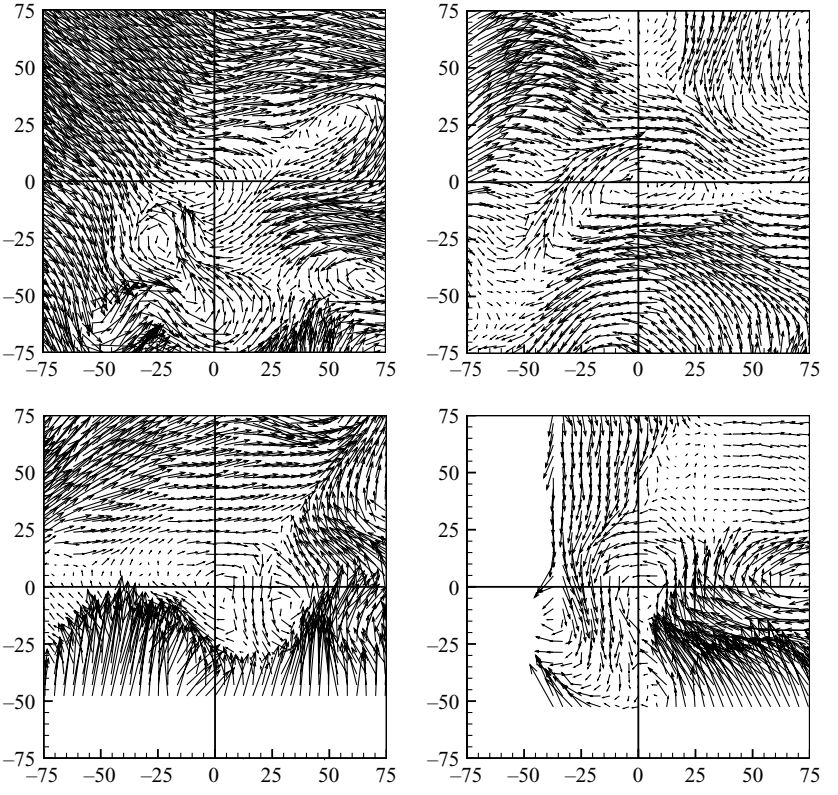

FIGURE 23. Examples of rejected eddy structures in the $(\boldsymbol{e}_z, \boldsymbol{e}_u)$-plane at $R_\theta = 7500$.

here. They can be found in Carlier (2001). It will just be mentioned that, concerning the flow structure, these results are in fair agreement with those of these authors (see final discussion) except for one point. In the present study, a large number of eddy structures with positive vorticity (opposite to that of the mean flow) were detected (see table 6). This was first pointed out by Falco (1974) in his visualization studies which led to his model of typical eddies (Falco 1983). In fact, these counter-rotating eddies are here half as numerous as the negative ones, but with nearly the same mean characteristics (size and intensity). This leads to the conclusion that both could belong to the same distorted vortex tube, or at least have the same origin. However, this observation was done previously at high Reynolds number and in the logarithmic region. It should be expected that fewer of these positive eddy structures exist very near to the wall. This will be confirmed by the present results.

4.1. *Averaged eddy structure*

All the eddy structures detected were extracted from the velocity maps. In each extracted sample, one eddy structure is centred. The instantaneous convection velocity (determined by the least-squares fitting) of the eddy structure was subtracted from the sample. The eddy structures which have their centre located in the same layer of thickness $\Delta y^+ = 24$ were averaged together. Figures 24, 25 and 26 present the in-plane components of the velocity corresponding to these averaged eddy structures at different wall distances, respectively, in the planes $(\boldsymbol{e}_z, \boldsymbol{e}_u)$, $(\boldsymbol{e}_z, \boldsymbol{e}_y)$ and $(\boldsymbol{e}_z, \boldsymbol{e}_d)$

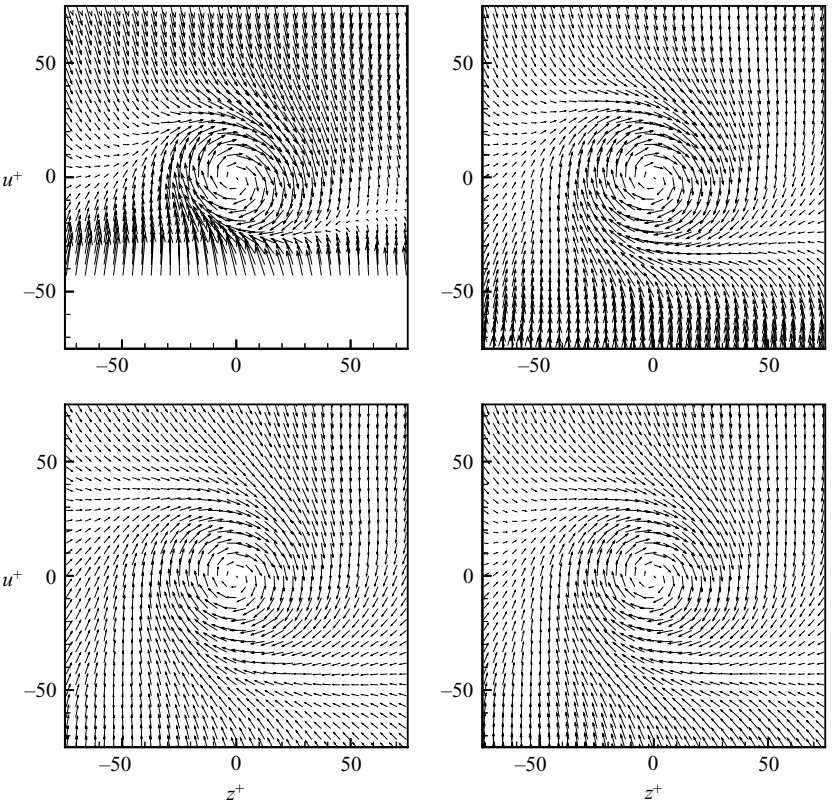

FIGURE 24. Averaged eddy structures in the $(\boldsymbol{e}_z, \boldsymbol{e}_u)$ upstream tilted plane at $R_\theta = 7500$: ${y_o}^+ = 50$, 75, 100 and 125 (clockwise from the top left-hand side).

at $R_\theta = 7500$. Note should be taken of the fact that the averaging procedure of a large number of more or less isotropic structures such as those of figure 22 tends to make the 'averaged' structure more isotropic. This has the advantage, in a first step, of providing a single length and velocity scale to characterize the vortices under study.

In figure 24, note that the $(\boldsymbol{e}_z, \boldsymbol{e}_u)$-plane is inclined at 45° upstream. Thus, subtracting the convection velocity at the centre of the eddy structure, owing to the projection of the strong mean velocity gradient along y, leads to an apparent converging motion toward the horizontal axis. Nevertheless, the eddy structures are strong enough to appear clearly. The averaged eddy structure located around ${y_o}^+ = 50$ does not have an isotropic shape because of the viscous interaction with the wall. This effect disappears away from the wall and the shape evolves toward an apparent isotropic spiral pattern which converges toward the centre.

In figure 25, the out-of-plane component of the velocity is available because 2D3C PIV was used. The grey levels give the streamwise component of the velocity minus the mean value of the vortices convection velocity. The averaged eddy structures are very similar to those in the $(\boldsymbol{e}_z, \boldsymbol{e}_u)$-plane. The one located at ${y_o}^+ = 50$ develops a lift-up motion in a region of low longitudinal velocity on the lower left-hand side and a sweeping motion in a region of high longitudinal velocity on the upper right-hand side. Note the transverse motion of 'sweep' type, occurring along the wall just under

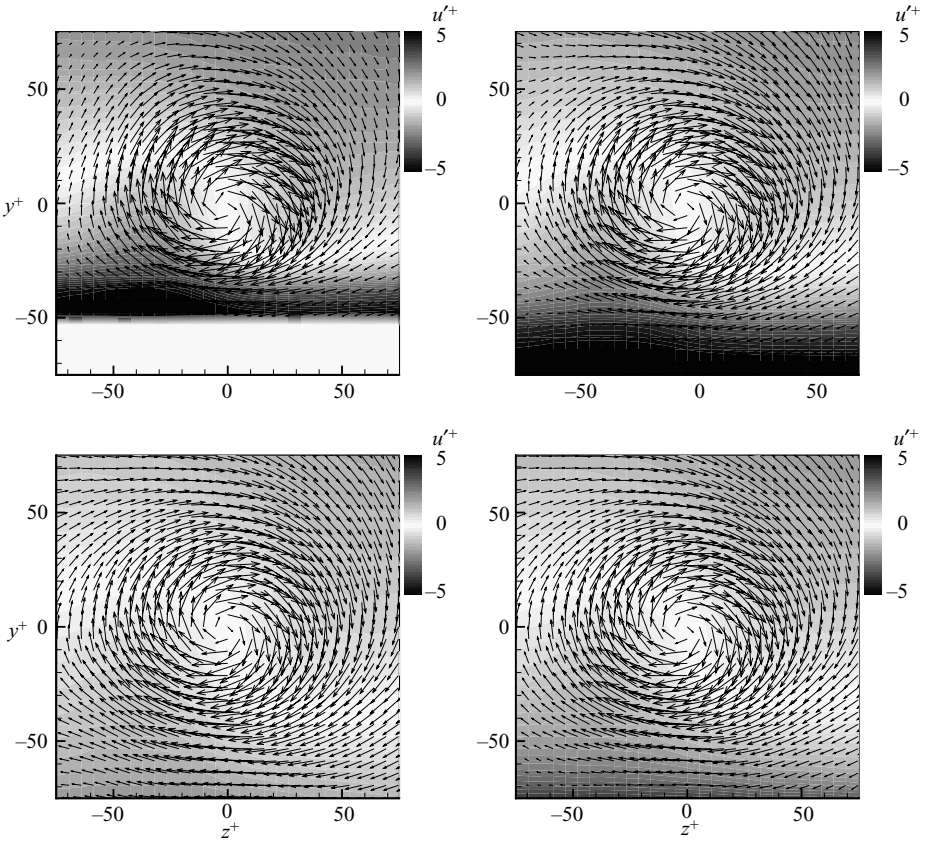

FIGURE 25. Averaged eddy structures in the $(\boldsymbol{e}_z, \boldsymbol{e}_y)$ normal to the wall plane at $R_\theta = 7500$: ${y_o}^+ = 50$, 75, 100 and 125 (clockwise from the top left-hand side). The grey scale gives the out-of-plane component.

this averaged eddy structure. Such motions are also clearly visible in the $(\boldsymbol{e}_x, \boldsymbol{e}_z)$-plane parallel to the wall (not shown here).

In figure 26, the same phenomenon (due to the projection of the mean velocity gradient) as in figure 24 appears, but this time with a diverging motion away from the centre of the eddy (owing to the downstream tilt angle of the plane of observation). The averaged eddy structures obtained do not differ from the previous ones as far as the size and intensity are concerned. Table 6 shows nevertheless that they are much less numerous (this will be discussed in the next section).

4.2. *Number of eddy structures*

To give an order of magnitude, the mean number of eddy structures detected in each velocity map is about 6 in the $(\boldsymbol{e}_z, \boldsymbol{e}_u)$-plane, about 14 in the $(\boldsymbol{e}_z, \boldsymbol{e}_y)$-plane (the field of view is four times larger) and about 1 in the $(\boldsymbol{e}_z, \boldsymbol{e}_d)$-plane. To study the behaviour of the number of eddy structures detected as a function of the wall distance, and to compare these data for various light sheet orientations, the wall distance was stratified in layers, each with a thickness of 24^+. The number of eddy structures having their centre in each layer is divided by the layer surface. The value obtained is called the density of eddy structures in the layer.

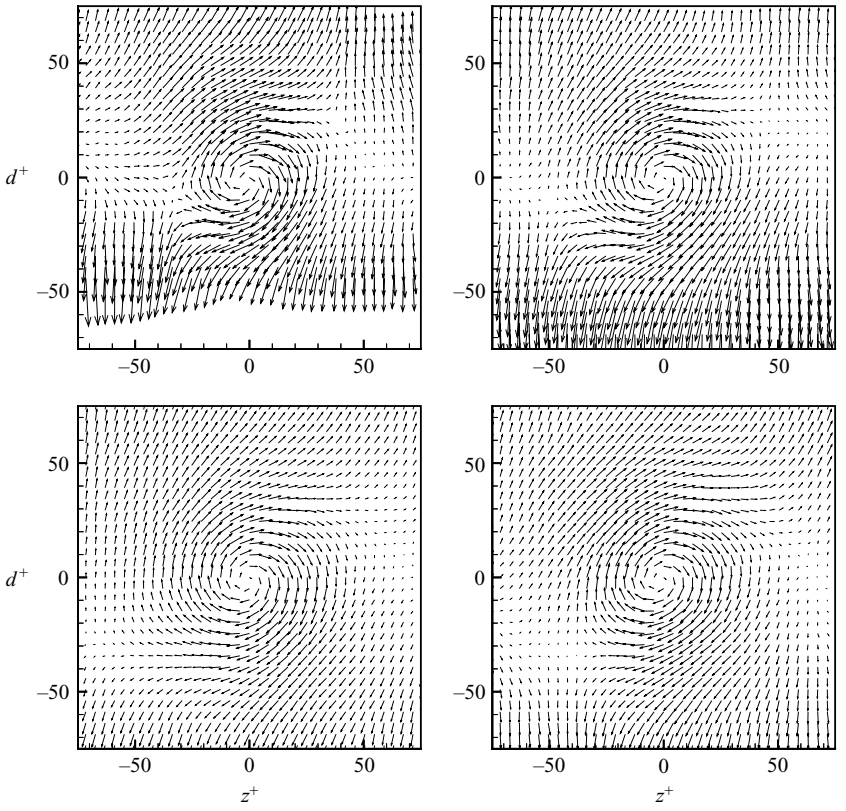

FIGURE 26. Averaged eddy structures in the $(\boldsymbol{e}_z, \boldsymbol{e}_d)$ downstream tilted plane at $R_\theta = 7500$: ${y_o}^+ = 50$, 75, 100 and 125 (clockwise from the top left-hand side).

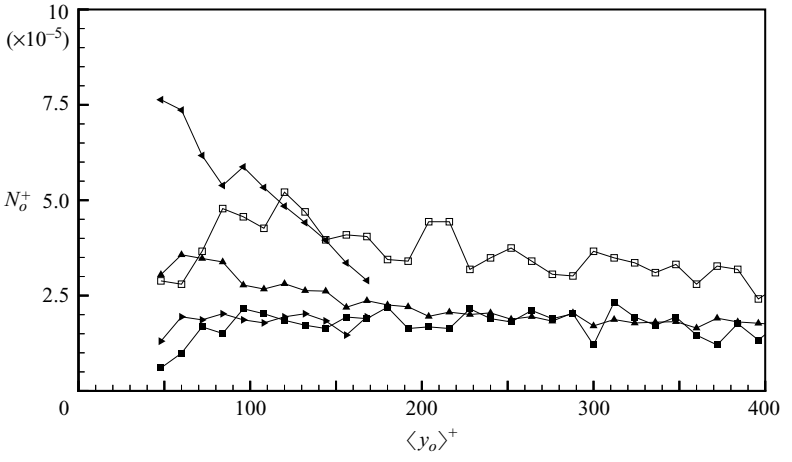

FIGURE 27. Density profiles of eddy structures in various planes at $R_\theta = 7500$: □, $(\boldsymbol{e}_x, \boldsymbol{e}_y)$-plane and $\omega_o < 0$; ■, $(\boldsymbol{e}_x, \boldsymbol{e}_y)$-plane and $\omega_o > 0$; ▲, $(\boldsymbol{e}_z, \boldsymbol{e}_y)$-plane; ◄, $(\boldsymbol{e}_z, \boldsymbol{e}_u)$-plane; ►, $(\boldsymbol{e}_z, \boldsymbol{e}_d)$-plane.

Figure 27 presents this density for various plane orientations at $R_\theta = 7500$ and as a function of the wall distance. The identification method used did not allow us to detect eddy structures with a centre lower than 40^+ because of the size of the damping radius.

In the $(\boldsymbol{e}_x, \boldsymbol{e}_y)$-plane, the two types of eddy structure ($\omega_o < 0$ and $\omega_o > 0$) are presented as they correspond to a different interpretation (no homogeneity hypothesis in that plane as in planes containing the z-axis). It appears clearly in this plane that the eddy structures rotating in the natural sense ($\omega_o < 0$) are at least twice as numerous than the counter-rotating one ($\omega_o > 0$).

In the three transverse planes, it has been checked first that the eddy structure, with both signs of vorticity are in equivalent quantity. Herein, only the eddy structures with the same sign of vorticity are presented. The $(\boldsymbol{e}_z, \boldsymbol{e}_u)$-plane shows clearly a peculiar behaviour. The number of detected eddy structures is obviously increasing rapidly when approaching the wall. On the contrary, in the $(\boldsymbol{e}_z, \boldsymbol{e}_d)$-plane, the total number is much smaller and it decreases toward the wall. Also, the data in these two tilted planes are available only up to $y^+ = 180$. Above this wall distance, an evolution toward some kind of equiprobability would lead the number of eddy structures in both tilted planes to converge toward the same value $(N_o{}^+ = (\mathrm{n/S})(\nu u_\tau)^2 \simeq 2\ 10^{-5})$ around $y^+ = 180$.

In the $(\boldsymbol{e}_z, \boldsymbol{e}_y)$-plane, the behaviour is comparable to the $(\boldsymbol{e}_z, \boldsymbol{e}_u)$-plane; the number of eddy structures is again increasing toward the wall, but they are about half as numerous as compared to the $(\boldsymbol{e}_z, \boldsymbol{e}_u)$-plane. Above $y^+ \simeq 180$, based on a reasonable equiprobability hypothesis, we can expect all curves, except the one for $\omega_o < 0$ in the $(\boldsymbol{e}_x, \boldsymbol{e}_y)$-plane, to converge to the same and more or less constant value of $N_o{}^+ \simeq 2 \times 10^{-5}$. The region under investigation can then be separated into two sub-regions:

(i) Above $y^+ = 180$, the number of eddy structures detected is the same in all planes except for $\omega_o < 0$ in the $(\boldsymbol{e}_x, \boldsymbol{e}_y)$-plane. These last eddies are more or less twice as numerous as the others and their population is slowly decreasing with the wall distance (while the others remain relatively constant in the field of view). An extrapolation of the curves leads to the conclusion that we should come to a kind of isotropy of the vortex distribution at $y^+ \simeq 800$, which is the limit between the logarithmic and the wake region in the present case. The fact that the number of $\omega_o < 0$ eddy structures is about twice the number of eddy structures of one sign in the $(\boldsymbol{e}_z, \boldsymbol{e}_u)$- and $(\boldsymbol{e}_z, \boldsymbol{e}_y)$-planes indicates that statistically one head is more or less associated to one leg (of either sign) in this region, thus arguing more in favour of the cane hypothesis that the hairpin one.

(ii) In the range, $40 < y^+ < 180$, the situation is more complex. The number of eddy structures detected in the $(\boldsymbol{e}_z, \boldsymbol{e}_u)$-plane increases rapidly toward the wall, while the number in the $(\boldsymbol{e}_z, \boldsymbol{e}_d)$-plane is nearly constant and finally decreases very near to the wall. Taking into account the fact that the detector used somehow favours eddy structures normal to the corresponding plane, this result supports the hypothesis that the eddy structures in this region are preferably tilted at more or less 45° downstream to the wall. This hypothesis is somewhat contradicted by the results in the $(\boldsymbol{e}_z, \boldsymbol{e}_y)$-plane which does not increase toward the wall as fast as those in the $(\boldsymbol{e}_z, \boldsymbol{e}_u)$-plane (a vortex at 45° downstream should cut the $(\boldsymbol{e}_z, \boldsymbol{e}_y)$-plane). This contradiction is not so strong if we take into account the fact that, if these vortices are really at an angle of 45° to the wall, they should appear fairly elliptic in the $(\boldsymbol{e}_z, \boldsymbol{e}_y)$-plane and be, at least partly, eliminated by the present detector. The last interesting result in this region is the strong decrease toward the wall of the number of eddy structures of both signs detected in the $(\boldsymbol{e}_x, \boldsymbol{e}_y)$-plane indicating that the number of cane vortices is decreasing toward the wall, in favour of eddy structures forming small angles with the $(\boldsymbol{e}_x, \boldsymbol{e}_y)$-plane.

Figure 28 gives the same quantity in the $(\boldsymbol{e}_z, \boldsymbol{e}_u)$-plane as a function of the Reynolds number. This result, confirms the evolution observed in figure 27 (a significant increase

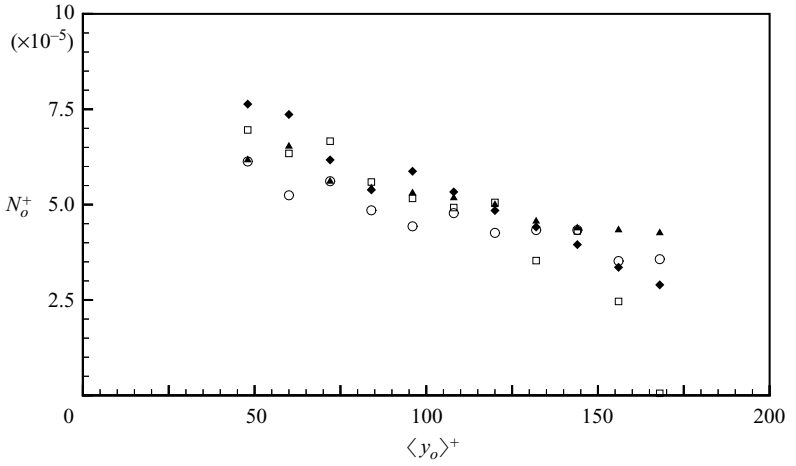

FIGURE 28. Density profiles of eddy structures in the $(\boldsymbol{e}_z, \boldsymbol{e}_u)$-plane: ◆, $R_\theta = 7500$; □, $R_\theta = 10\,500$; ▲, $R_\theta = 13\,500$; ○, $R_\theta = 19\,000$.

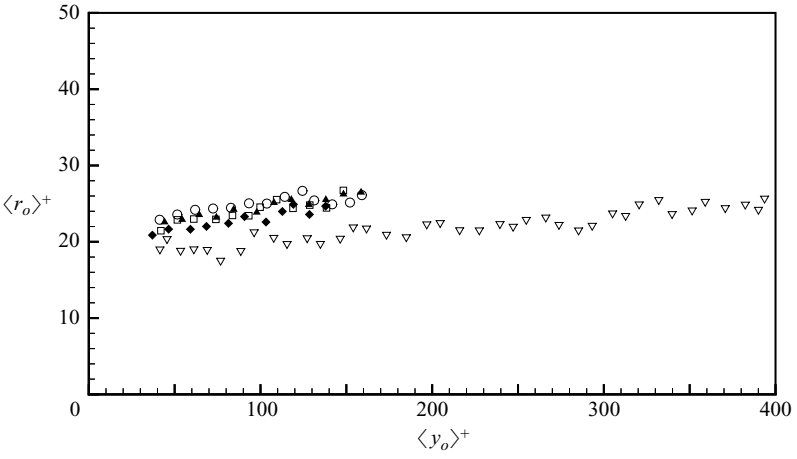

FIGURE 29. Mean radius profiles of eddy structures: ▽, $(\boldsymbol{e}_x, \boldsymbol{e}_y)$-plane and $R_\theta = 7500$; ◆, $(\boldsymbol{e}_z, \boldsymbol{e}_u)$-plane and $R_\theta = 7500$; □, $(\boldsymbol{e}_z, \boldsymbol{e}_u)$-plane and $R_\theta = 10\,500$; ▲, $(\boldsymbol{e}_z, \boldsymbol{e}_u)$-plane and $R_\theta = 13\,500$; ○, $(\boldsymbol{e}_z, \boldsymbol{e}_u)$-plane and $R_\theta = 19\,000$.

of the number of eddies in this plane) at all Reynolds numbers. Looking carefully at the results, a different slope is observed between the group $R_\theta = 7500$ and 10 500 and the group $R_\theta = 13\,500$ and 19 000. It is not clear at the present stage whether this should be interpreted as a Reynolds-number dependence or attributed to a lack of statistical convergence.

4.3. *Mean characteristics*

Figures 29 and 30 show the mean radius and the mean vorticity profiles of the eddy structures at four Reynolds numbers in the $(\boldsymbol{e}_z, \boldsymbol{e}_u)$-plane and at $R_\theta = 7500$ in the $(\boldsymbol{e}_x, \boldsymbol{e}_y)$-plane. These two quantities appear relatively universal in wall units.

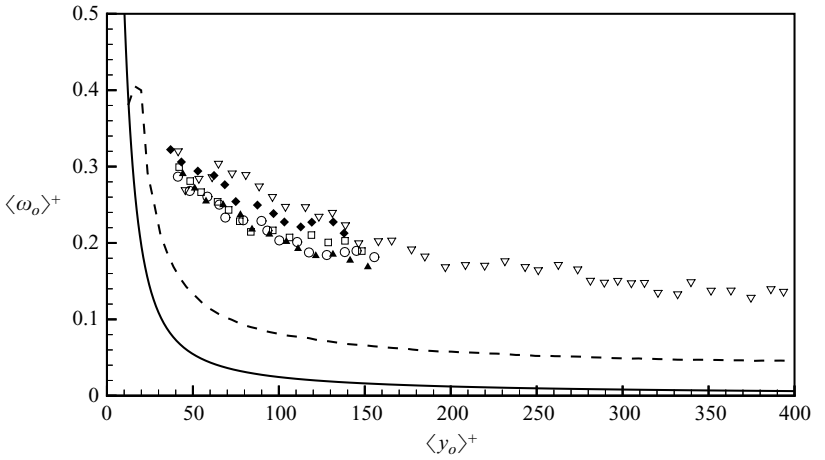

FIGURE 30. Mean vorticity profiles of eddy structures: ▽, $(\boldsymbol{e}_x, \boldsymbol{e}_y)$-plane and $R_\theta = 7500$; ◆, $(\boldsymbol{e}_z, \boldsymbol{e}_u)$-plane and $R_\theta = 7500$; □, $(\boldsymbol{e}_z, \boldsymbol{e}_u)$-plane and $R_\theta = 10\,500$; ▲, $(\boldsymbol{e}_z, \boldsymbol{e}_u)$-plane and $R_\theta = 13\,500$; ○, $(\boldsymbol{e}_z, \boldsymbol{e}_u)$-plane and $R_\theta = 19\,000$; - - -, r.m.s. spanwise vorticity; ———, Van Driest profile.

In the $(\boldsymbol{e}_z, \boldsymbol{e}_u)$-plane, the mean radius increases slowly away from the wall, starting from about 20^+ at $y^+ = 40$ and with a mean value of about 24^+ in the region of investigation. By contrast, the mean vorticity decreases slowly. The combination of both keeps the circulation (defined by $\langle \Gamma_o \rangle = 2\pi \langle \omega_o r_o^2 \rangle$ in the case of an Oseen vortex) almost constant in wall units ($\langle \Gamma_o \rangle^+ / 2\pi = 140$). The mean vorticity profiles, extrapolated toward the wall, intersects the ω_z' profile around $y^+ = 25$, which corresponds to the peak of this quantity (the peak of ω_x' being nearby at $y^+ = 20$). At this wall distance, ω_z' is about twice the mean velocity gradient $\partial U / \partial y$ (which represents the main component of the mean vorticity). This supports the idea that the vortical structures observed further away from the wall have their origin around $y^+ = 25$, in the region of the strongest vorticity fluctuation, with an initial radius around 20^+ which places them just above the viscous sublayer.

In the $(\boldsymbol{e}_x, \boldsymbol{e}_y)$-plane, the size of the vortex heads is starting from the same near-wall value. It slowly increases (almost linearly) with wall distance, leading to a slightly smaller mean value ($\sim 22^+$). The vorticity of the heads is slightly higher and remains significant away from the wall. The circulation is somewhat smaller ($\langle \Gamma_o \rangle^+ / 2\pi = 100$). It decreases slowly and linearly away from the wall. The results in the two other planes (not shown) agree well with those presented. Globally, we can conclude that the mean radius $\langle r_o \rangle^+$ of the vortices varies between 20 and 30 and increases slowly away from the wall while the mean circulation $\langle \Gamma_o \rangle^+ / 2\pi$ varies between 80 and 150 in the different planes and is almost constant (or very slowly linearly decreasing) through the region of observation.

To conclude, figure 31 gives the mean convection velocity of the eddy structures in the $(\boldsymbol{e}_z, \boldsymbol{e}_y)$-plane as a function of the wall distance (available thanks to the use of a stereoscopic PIV measurements). This convection velocity, which is provided by the least-squares procedure, is compared to the mean velocity profile proposed by Van Driest. As can be seen, the difference between them is very small. This result, which was already approached by a visualization study by Hoyez-Delaliaux (1990), is in good agreement with Adrian *et al.* (2000*b*). The latter authors find very good coincidence between the convection velocity of the vortices and the mean velocity

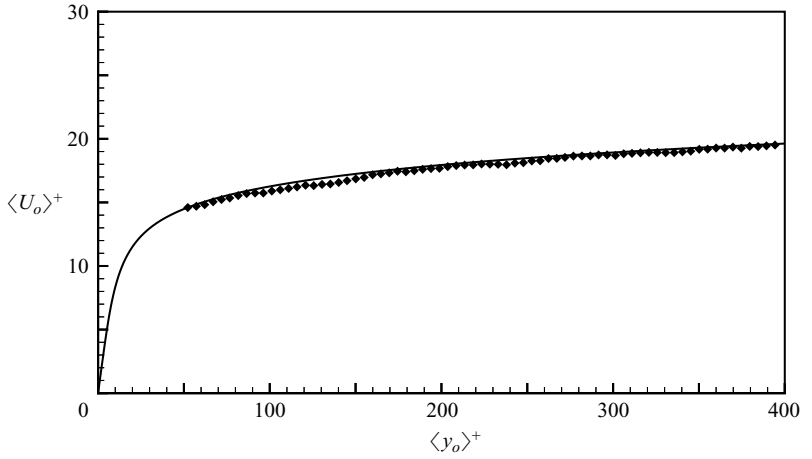

FIGURE 31. Mean convection velocity of eddy structures in the $(\boldsymbol{e}_z, \boldsymbol{e}_y)$-plane: ◆, $R_\theta = 7500$; ———, Van Driest profile.

profile up to $y^+ = 800$ at $R_\theta = 7500$, which is in agreement with the present results. Farther from the wall, the convection velocity measured by Adrian *et al.* (2000*b*) becomes smaller than the mean and more scattered. Looking at the number of samples used, we may question the convergence of their results in this outer region where the vortices are less numerous. This result on the convection velocity in the log region has recently been confirmed by Christensen & Adrian (2002). The same results (not shown) are obtained in the $(\boldsymbol{e}_x, \boldsymbol{e}_y)$-plane together with a very good universality in wall units for $50 < y^+ < 500$ and for the four Reynolds numbers.

4.4. *Spatial relationships between coherent structures*

It is commonly assumed that the low-speed streaks come from the interaction of the eddy structures with the wall and that their lift-up causes the formation of ejections responsible for the turbulent kinetic energy production (see Kim, Kline & Reynolds 1971). The relationships between these various types of coherent structure can be revealed by building the indicative functions of the regions occupied by each of them in the velocity maps. These indicative functions are binary functions in the plane of interest. They take the value 1 at a point inside a corresponding coherent structure and the value 0 elsewhere. The relationships investigation is possible especially with the 2D3C PIV measurements performed in the $(\boldsymbol{e}_z, \boldsymbol{e}_y)$-plane. The indicative functions of different coherent structures are cross-correlated with each other to give the probability map of the location of one (at the moving point) compared to the other (at the fixed point). To improve the convergence, the fixed point was moved along the transverse direction and the cross-correlation maps obtained were averaged together around the fixed point (to take advantage of the homogeneity of the flow in that direction). Consequently, the convergence decreases as the moving point is moved away from the fixed point in the transverse direction. The probability maps obtained for various coherent structures are shown in figures 32 to 37.

The regions occupied by the eddy structures in the indicative function should have a size proportional to the size of the eddy structures themselves. As was observed, r_o does not vary too much (see figure 19), and to simplify the processing, a circular region with a constant radius equal to the damping radius σ was selected for all the eddy structures.

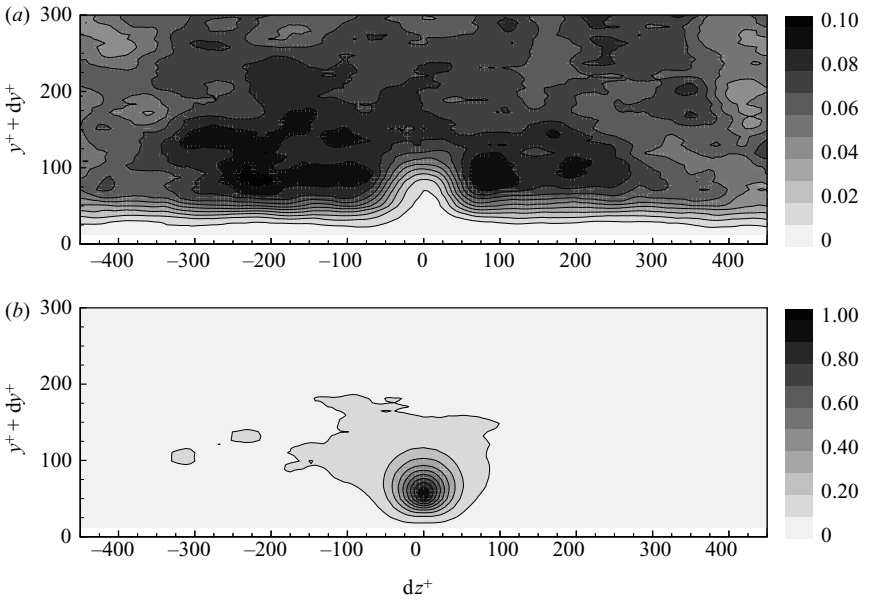

FIGURE 32. Probability map of the location of negative eddy structure and positive eddy structure compared to positive eddy structure at $y^+ = 50$ and $R_\theta = 7500$ in the $(\boldsymbol{e}_z, \boldsymbol{e}_y)$-plane. (*a*) Fixed point, positive eddy structure; moving point, negative eddy structure. (*b*) Fixed point, positive eddy structure; moving point, positive eddy structure.

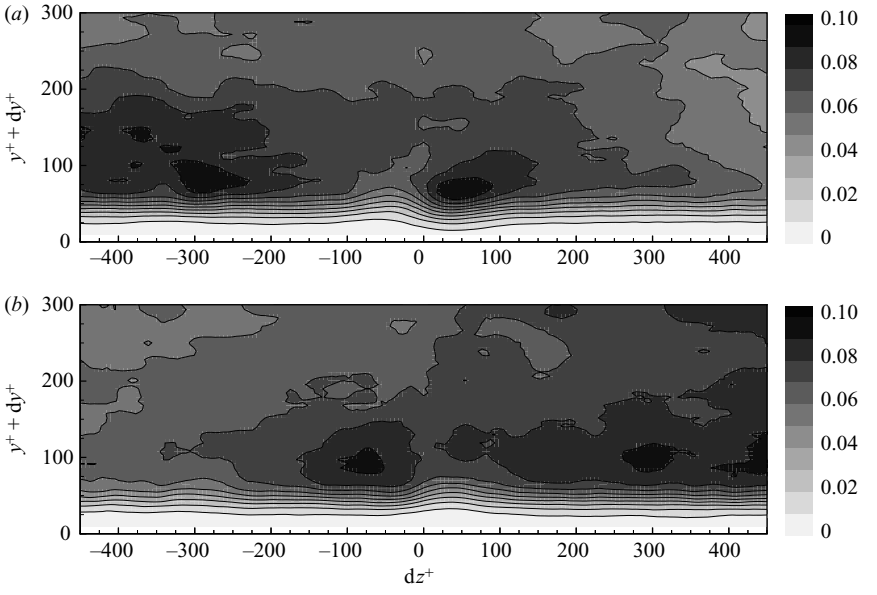

FIGURE 33. Probability map of the location of positive eddy structure compared to high-speed streak and low-speed streak at $y^+ = 15$ and $R_\theta = 7500$ in the $(\boldsymbol{e}_z, \boldsymbol{e}_y)$-plane. (*a*) Fixed point, high-speed streak; moving point, positive eddy structure. (*b*) Fixed point, low-speed streak; moving point, positive eddy structure.

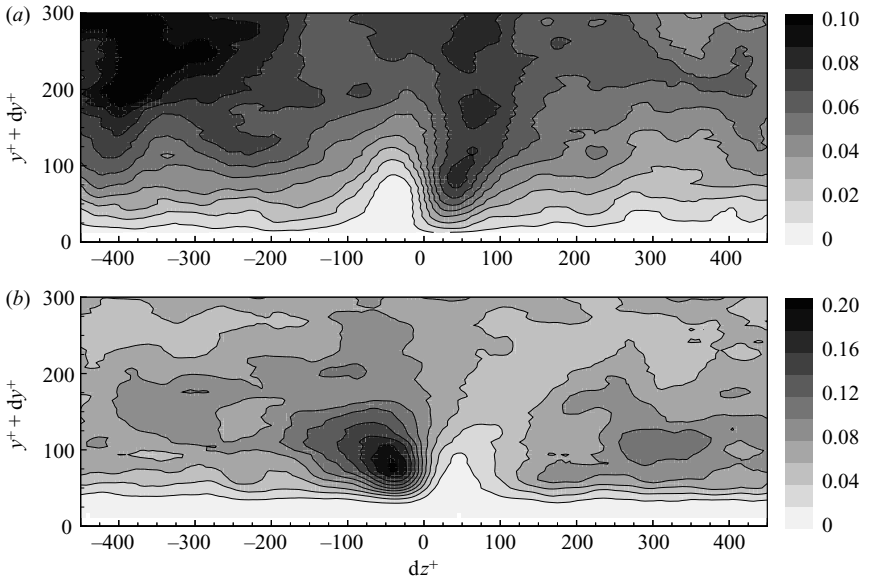

FIGURE 34. Probability map of the location of ejection compared to positive eddy structure and positive eddy structure compared to ejection at $y^+ = 50$ and $R_\theta = 7500$ in the $(\boldsymbol{e}_z, \boldsymbol{e}_y)$-plane. (*a*) Fixed point positive eddy structure; moving point, ejection. (*b*) Fixed point, ejection; moving point, positive eddy structure.

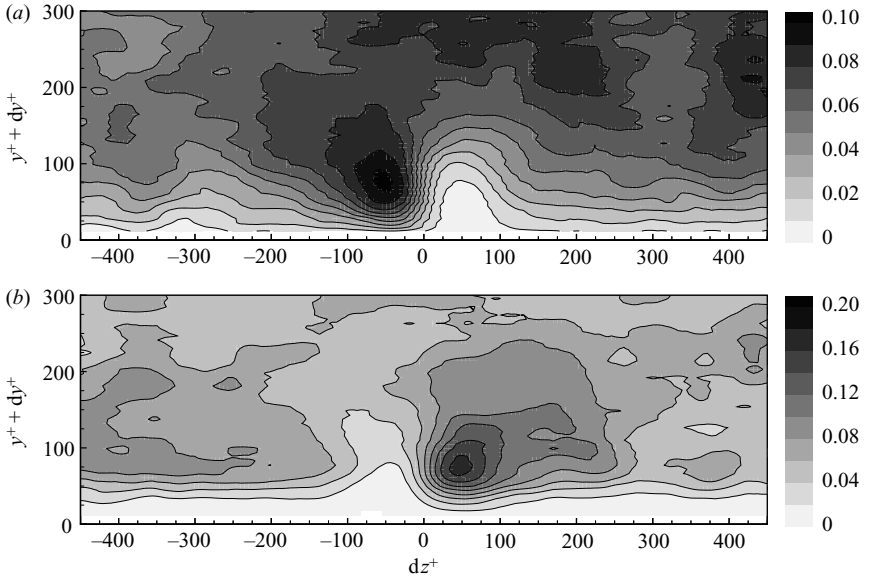

FIGURE 35. Probability map of the location of sweep compared to positive eddy structure and positive eddy structure compared to sweep at $y^+ = 50$ and $R_\theta = 7500$ in the $(\boldsymbol{e}_z, \boldsymbol{e}_y)$-plane. (*a*) Fixed point, positive eddy structure; moving point, sweep. (*b*) Fixed point, sweep; moving point, positive eddy structure.

The indicative functions of the regions occupied by the ejections in a velocity map are obtained according to the quadrant method by Wallace, Eckelmann & Brodkey (1972). The detection variable for the ejections (corresponding to the second quadrant

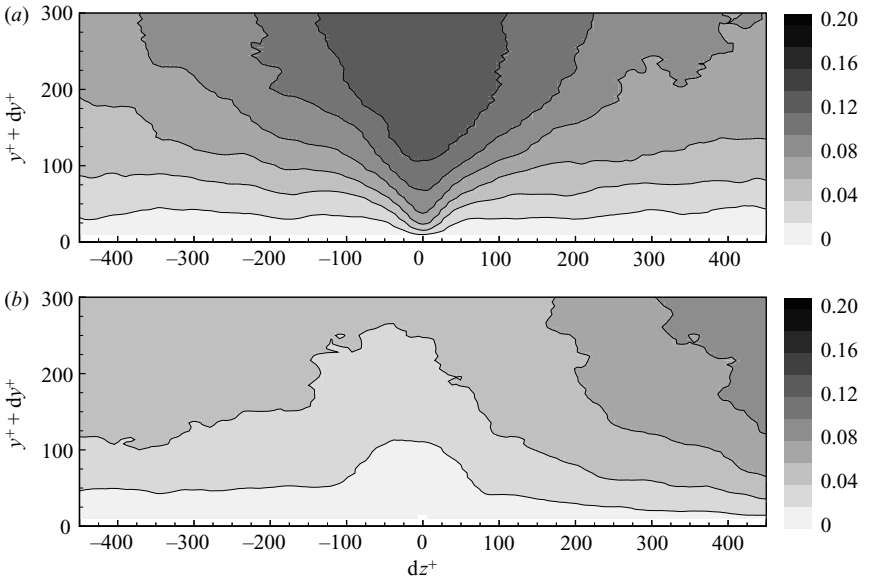

FIGURE 36. Probability map of the location of ejection and sweep compared to low speed streak at $y^+ = 15$ and $R_\theta = 7500$ in the $(\boldsymbol{e}_z, \boldsymbol{e}_y)$-plane. (*a*) Fixed point, low-speed streak; moving point, ejection. (*b*) Fixed point, low-speed streak; moving point, sweep.

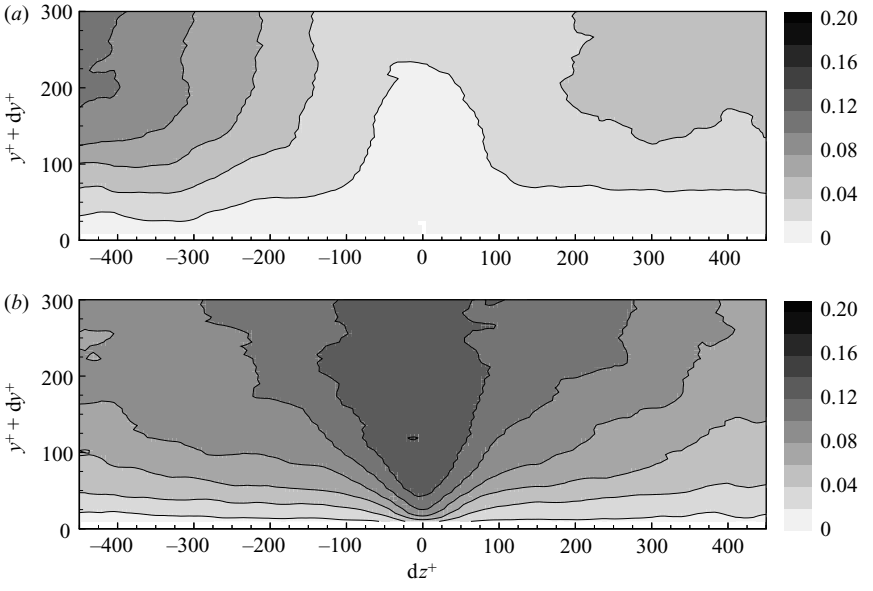

FIGURE 37. Probability map of the location of ejection and sweep compared to high-speed streak at $y^+ = 15$ and $R_\theta = 7500$ in the $(\boldsymbol{e}_z, \boldsymbol{e}_y)$-plane. (*a*) Fixed point, high-speed streak; moving point, ejection. (*b*) Fixed point, high-speed streak; moving point, sweep.

in the joint probability density function of u' and v') was chosen as the instantaneous Reynolds shear stress $u'v'$, normalized by the local standard deviation product $\sigma_u \sigma_v$. The detection function is the map of the detection variable. The indicative function

is the detection function thresholded at a level H and binarized. As in Wallace, Eckelmann & Brodkey (1972), a value of $H = 1$ was chosen.

The characteristic variable of the streaks is the longitudinal velocity fluctuation u'. Therefore it is natural to choose it, normalized by the local variance σ_u, as the detection variable. The detection function for the low-speed streaks is the negative part of the detection variable (and vice versa for the high-speed streaks). The indicative function is the detection function thresholded by H and binarized. There are no references to provide guidance for the best value of H, but $H = 1$ appeared to suit very well in the present case.

4.4.1. *Eddy structures*

Figure 32(a) gives the probability of finding a negative eddy structure (clockwise) in the field of view when a positive one (counterclockwise) is located at $y^+ = 50$ in the $(\boldsymbol{e}_z, \boldsymbol{e}_y)$-plane at $R_\theta = 7500$. Figure 32(b) gives the same probability, but with two positive eddy structures. It is clear from these two diagrams that the most probable situation, which is fairly weak (about 10 %), is to have counter-rotating adjacent eddy structures near the wall separated in the spanwise direction. Note that the fixed point is at $y^+ = 50$, which is the nearest possible to the wall with this data set and which is the outer limit of the buffer-layer. Taking into account the mean radius of the eddy structures at this wall distance (23^+), they penetrate deep into this buffer-layer (see figure 25).

4.4.2. *Eddy structures – streaks*

Figure 33(a) gives the probability of finding a positive eddy structure in the field of view when a high-speed streak is located at $y^+ = 15$ in the $(\boldsymbol{e}_z, \boldsymbol{e}_y)$-plane. A peak is clearly observable in the immediate vicinity of the high-speed streak, showing that eddy structures are relatively often associated with these streaks. This is true also for low-speed streaks, as illustrated by figure 33(b) (but with a maximum of correlation slightly farther in the transverse direction: 75^+ instead of 50^+). The second peak appearing on both diagrams at $dz^+ \sim 300$ should be looked at with caution, as the convergence is not as good near the border of the field of view. However, although the known size difference in the longitudinal direction (200^+ for the vortical structures at the wall and 1000^+ for the low speed streaks, see Kim *et al.* (1987), the level and the size of the regions of highest probability in figures 33(a) and 33(b) indicate that the chances that the $(\boldsymbol{e}_z, \boldsymbol{e}_y)$-plane cuts these two types of coherent structure (vortices and streaks) simultaneously are fairly high.

4.4.3. *Eddy structures – ejections and sweeps*

Figure 34(a) gives the probability of finding an ejection in the field of view when a positive eddy structure is located at $y^+ = 50$ in the $(\boldsymbol{e}_z, \boldsymbol{e}_y)$-plane. A region of ejection, with a probability of 10 %, is clearly evidenced at the right-hand side of the eddy structures, starting very near the vortex (of radius 23^+) and extending from the wall to $y^+ = 300$. This means that the chances to have an ejection associated to an eddy near the wall are high. The complementary correlation is given in figure 34(b) (ejection at the fixed point and positive eddy structures at the moving point). As can be observed, the correlation peak is significantly stronger here and much more localized. Although the local probability is not very high in these maps, the region at this level is wide enough to expect, for example, in figure 34(b) a vortex to be centred somewhere inside it with a fairly high probability. This does not exclude the fact that other types of coherent structure can be well correlated with an ejection, but

it shows at least that coherent vortex structures are fairly often linked to this event. The two diagrams of figure 34 indicate that the probability of an eddy structure being closely tied to an ejection is less than for an ejection to be directly linked to an eddy structure.

Figures 35 shows the same correlations as in figure 34, but now for a sweep instead of an ejection. The direct link between an eddy structure and a sweep appears stronger than for an ejection in figure 34(*a*). Again, the probability is higher for a sweep to be associated to an eddy structure than the contrary.

4.4.4. *Streaks – ejections and sweeps*

Figure 36 gives the probability of finding an ejection or a sweep in the field of view when a low-speed streak is located at $y^+ = 15$ in the $(\boldsymbol{e}_z, \boldsymbol{e}_y)$-plane. The same data are given in figure 37 for high-speed streaks. These four diagrams illustrate clearly the well-known relation existing between low-speed streaks and ejections on one hand and high-speed streaks and sweeps on the other hand. It should nevertheless be noted that the level of correlation obtained leaves room for low-speed streaks without ejections and high-speed streaks without sweeps. This point cannot be confirmed here as the corresponding complementary correlation is not accessible within the present data set.

5. Discussion

The aim of the present contribution was to take advantage of PIV to bring some new experimental information to the characterization and the understanding of the near-wall coherent structures at high Reynolds number. After presenting the data obtained and the main immediate insights that they can bring, it is important to situate and discuss them with respect to the present understanding of near-wall turbulence. Looking at the large number of publications since Theodorsen (1952), this seems a giant task. Thankfully, this problem, which is of strong interest for the turbulence community, has been reviewed from time to time. This discussion refers to the review by Panton (1997). Most of the teams working on near-wall turbulence contributed to this book, summarizing their views on the flow organization in this region. Not all of these contributions will be detailed in the discussion. Only those based on the types of data comparable to those provided in the present contribution (mostly DNS and PIV) will be addressed in detail here (Smith & Walker 1997; Hanratty & Papavassiliou 1997; Kline & Portela 1997; Schoppa & Hussain 1997). Concerning the team of Adrian, a more recent paper (Christensen & Adrian 2002) has appeared and is more relevant. In addition, the Schoppa & Hussain (1997) point of view has been laid out in Schoppa & Hussain (2002). Apart from the Adrian group which has an experimental approach similar to the present one, most of these workers obtained their knowledge mainly from DNS or experiments at low Reynolds numbers. It is thus of interest to see how the present data corroborate, or not, their results for higher Reynolds numbers. Moreover, several of these workers focused particularly on the very near-wall region, to try to understand the self-sustaining mechanism in the buffer-layer. Although the present measurements could not go deep into this region (except data not shown in the $(\boldsymbol{e}_x, \boldsymbol{e}_z)$-plane), it is of interest to see how they agree with the different models proposed and their consequences away from the wall.

As far as these near-wall self-sustaining mechanisms are concerned, it should be recalled, as was emphasized by Schoppa & Hussain (2002), that they can be classified

in two categories: those based on a parent–offspring scenario (see Smith & Walker 1997; Hanratty & Papavassiliou 1997), which suppose that new vortices are generated by the interaction of older vortices with the wall, and those based on an instability mechanism (see Kline & Portela 1997; Schoppa & Hussain 1997), which suppose that the vortices are generated mainly by an instability of the near-wall low-speed streaks. Up to now, most models of the second type rely on a shear-layer type of instability generating horseshoe or hairpin vortices. Schoppa & Hussain (2002) have now proposed a streak transient growth mechanism generating staggered and overlapping alternate quasi-streamwise vortices.

Looking at the present results, one of the most significant ones is that all the physical characteristics of the vortices (size, intensity, convection velocity) in the logarithmic region seem to scale in wall units. The only contributors addressing this point in Panton (1997) are Hanratty & Papavassiliou (1997), who come to the same conclusion for both the size and the velocity scale of the vortices. Moreover, they obtained a size of $2r_o^+ \simeq 50$ near the wall, which is in fair agreement with the one found here.

Christensen & Adrian (2002) also addressed this point for a channel flow, and came to a somewhat different conclusion that the spatial extent of the eddy structures is fairly constant in outer variable scaling. The first reason which could be invoked is that the present results are biased toward small eddy size owing to the small field of view. This does not stand analysis as the data in the $(\boldsymbol{e}_z, \boldsymbol{e}_y)$- and $(\boldsymbol{e}_x, \boldsymbol{e}_y)$-planes, which have a field of view in wall units comparable to that of Christensen & Adrian (2002) at $R_\tau = 550$, are in very good agreement with the planes having a smaller field of view. Three points can be made to explain this disagreement. (i) The spatial extent mentioned by Christensen & Adrian (2002) is not quantitatively defined and can be different from the radius used here. (ii) This spatial extent applies to an average eddy structure whereas we computed the average of the radius of individual structures. (iii) These authors mentioned that the same magnification (i.e. spatial resolution) was used for the PIV recording at the two Reynolds numbers in their study. This was also done at first in the present study and led to the same apparent conclusion. Because the size of the eddy structures diminishes in physical units when the Reynolds number increases, the spatial resolution has to be adapted to catch the PDF correctly on the small size side.

A second result concerns the characteristic scales of the eddy structures. Apart from near the wall, the vorticity of these eddies is much larger than the local mean shear stress ($\overline{U}_{x,y}$) and even the r.m.s. of ω_z. This vorticity decreases very slowly away from the wall, while the sizes of the vortices increase, but also very slowly. The result is that the circulation of the eddies is nearly constant all through the region of observation which extends from the top of the buffer-layer to the middle of the logarithmic region ($y^+ \simeq 500$). Although data are not available here to prove it, the extrapolation of the present results on the circulation indicates that the constancy of the circulation of the vortices should not change until at least the upper limit of the logarithmic region. A striking result is that this is true in all the planes of observation, that is for both 'legs' and 'heads'. Also striking is the fact that these eddies seem to have the same origin: the near-wall region around $y^+ = 25$, and a range of scale r_o^+ between 10^+ and 50^+ (standard deviation about 30 %) in the whole region of interest (see figure 19). As has been found previously (see Christensen & Adrian 2002) and as shown in figure 31, these eddies are convected on average with the local mean velocity. They thus evidence little self-induction, being submitted mainly to the mean shear stress.

One question which should be further discussed is that of the size and scaling of the eddy structures. In fact, the present results seem to contradict partly those obtained by Klewicki & Falco (1996) on the duration of ω_z events, using hot-wire anemometry. Based on a local Taylor hypothesis, a parallel can be made between the two scales (time and length). If the agreement is quite good in that these two scales are nearly constant in the range $50 < y^+ < 250$, Klewicki & Falco (1996) find that the duration of ω_z events does not scale in wall units, but with the Taylor micro time scale. First, it must be mentioned that both the Taylor-scale values and their Reynolds-number dependences are in reasonable agreement here with the data from these authors. This means that the present results do not scale with Taylor scales. Consequently, in the ω_z events detected by Klewicki & Falco (1996), there are events other than the present vortex structures, which scale differently from them. These events should most probably be local shear layers which have been filtered by the vortex detector used here.

Looking at Panton (1997), it is clear that this result on the scaling of the vortices contradicts some well-accepted ideas. Smith & Walker (1997), for example, are convinced that both hairpins and a majority of cane vortices travel near the wall in the outer part above the buffer-layer and send legs down toward the wall. The heads of these vortices are supposed to behave quite differently from the legs, that is, to expand and reduce their vorticity. That is to say, hairpin vortices evolve into similar, but much larger, vortices in the outer flow. The coalescence of smaller vortices into coherent structures of larger scale is also suggested. Vortex stretching is supposed to conserve the angular momentum $\omega^2 r$ while increasing the energy $\omega^2 r^2$, reducing the size and increasing dissipation. Here, the observed structures appear to nearly keep their circulation (ωr^2).

Hanratty & Papavassiliou (1997) come also to the conclusion that vortices grow significantly in size away from the wall (although the size they find near the wall is in fair agreement with the present result: 'turbulence production is controlled in the viscous wall region by vortical motions centred on average at $y^+ = 20$–25 and having a spanwise dimension of 40–50^+'). From their point of view, the stress-producing eddy structures in the viscous wall region are parts of vortical structures attached to the wall upstream, with a size of 10^+ along y and 20^+ along z (not detectable in the present data), which grow, tilt backward and eventually lift from the wall. They then increase in size and decrease in vorticity downstream until they disappear. Some of them reappear in the $(\boldsymbol{e}_x, \boldsymbol{e}_y)$-plane as spanwise heads.

The contribution of Kline & Portela (1997) is mainly based on the well-known analysis of the database of Spalart (1988) by Robinson (1991). They identify two families of vortices: tilted streamwise vortices near the wall (legs) and transverse vortices in the outer part (heads). Both are present in the logarithmic region and they are often connected on one side by a shoulder (very rarely on both sides $\sim 2\,\%$). They give no hint about the vortex size evolution away from the wall (see Robinson 1991), but find a diameter of about 50^+ near the wall, in agreement with Hanratty & Papavassiliou (1997). Schoppa & Hussain (2002) look in detail at the instability mechanism very near the wall in the buffer-layer, and give almost no indication about the logarithmic region. They come to a model of staggered vortices of opposite sign riding over the low-speed streaks and overlapping each other. These vortices are inclined at 9° to the wall in the $(\boldsymbol{e}_x, \boldsymbol{e}_y)$-plane and at $\pm 4°$ in the $(\boldsymbol{e}_x, \boldsymbol{e}_z)$-plane. They originate from an instability of the streaks. Their results and theory locate the origin of the vortices around $y^+ = 30$ with initial sizes of the order of 20^+ along y and z and 150^+ along x. These vortices are supposed to evolve rapidly into

arches, through a streaks instability → streamwise vortices → arch vortices mechanism instead of a streaks instability → arch vortices → streamwise vortices as inferred by Robinson (1991). No indication is given about the size of the heads, but their pictures from DNS data seem to indicate heads larger than the legs.

Apart from evident agreement with some results of each of these authors, the main contradiction between these results and the present data is that the size of the vortices is proposed to grow rapidly as they move outward. Two main reasons can be put forward to explain this discrepancy. The first possible reason is that the present analysis may have missed the larger vortices because they are not isotropic enough to fulfil the detection criterion. This reason is not supported by visual analysis of the data and also by the fact that Adrian *et al.* (2000*b*), using the same approach, come to a very similar estimation of the size of what they call the 'smallest' eddy structures. They also observe that this size is fairly constant throughout the boundary layer. The second possible reason to explain this discrepancy is that most of the conclusions of the other authors, described above, rely mainly on the analysis of DNS or experimental data at fairly low Reynolds number, where the logarithmic region is very small (or even does not exist). This is not the case for the present data (see figure 5). If it can be confirmed that the sizes of the vortices increase in the wake region at high Reynolds number, then the contradiction may not be as strong between the present results and the existing data. Besides, it should be mentioned that no evidence of coalescence was found directly in the present data (vortices were found to be fairly isolated), but the range of size observed ($10 < r_o{}^+ < 50$) leaves some room for such pairing to occur, especially near the wall where the rapid variation with the wall distance of the number of vortices in the $(\boldsymbol{e}_z, \boldsymbol{e}_u)$-plane suggests some pairing.

As a preliminary conclusion, we could tentatively define the upper limit of the low-Reynolds-number domain in wall turbulence as the situation where a clearly defined log layer exists to separate the buffer layer from the wake region. This situation should occur around $R_\theta = 2000$ for a boundary layer, which corresponds to about $Re_H = 20\,000$ for a channel flow (based on half-channel height and mean velocity). Above this value, comes the question of the Reynolds-number dependance of such a flow. This question is still open (even for the mean velocity profile), mainly due to the lack of accuracy on the wall shear stress measurement. If this proposal is true, the present data would be outside the range of low-Reynolds-number effect, whereas the data of Adrian *et al.* (2000*b*) would be on both sides and most of the DNS would be on the low-Reynolds-number side.

Before going further into the discussion of eddy structures, it would be worth summarizing the main results deduced from figure 27: above $y^+ = 180$, the mean number of heads is comparable to the total number of legs (of both signs) arguing for a cane configuration of the eddy structures in this region (but canes with a head size comparable to the leg size). A significant number of counter-rotating heads ($\omega_o > 0$) do appear in the $(\boldsymbol{e}_x, \boldsymbol{e}_y)$-plane (comparable to the number of legs in the transverse planes), with the same scales as the others. This is in agreement with the findings of Falco (1974), Klewicki & Falco (1996) and Kline & Portela (1997), but not supported by the data from Adrian. Between 50^+ and 180^+, eddy structures appear to be tilted downstream (around 45°) and streamwise-oriented (fewer heads) vortex tubes with a rapidly decreasing number away from the wall.

Summarizing the picture of eddy structures which emerge from the present data, we could say that the vortices in the logarithmic region are mainly canes of both sign, which scale in wall units. They find their origin near the wall, around $y^+ = 25$ and

evolve initially mainly as tilted streamwise vortices. They keep their circulation and evolve very slowly with wall distance while being convected at the local mean velocity. The number of vortices found in each map indicates that they are fairly sparse in space, supporting somehow the hypothesis of active/inactive motions. Comparing this picture to the above literature summary, it is clear that, apart from the size evolution with wall distance, it is in fair agreement with most of them. This agreement is particularly good with the model developed by Schoppa & Hussain (2002), except for two points. First, the heads appear much larger than the legs in the model. This can be explained by the low-Reynolds-number effect mentioned earlier and by the fact that the stretching should be much stronger at high Reynolds number and should counteract the diffusion and keep the vortex size growing slowly. Secondly, the model does not account for the counter-rotating heads observed in the experiment. This can also be explained by the fact that the model, as any model, is somewhat ideal. It gives angles of $\pm 4^\circ$ in the $(\boldsymbol{e}_x, \boldsymbol{e}_y)$-plane to the initial quasi-streamwise vortices and proposes that vortices of each sign tilt afterwards to generate canes with the right vorticity sign ($\omega_z < 0$). Taking into account the large standard deviation associated with all the characteristics of near-wall events (see Kline & Portela 1997), it can be expected that some of these initial quasi-streamwise vortices tilt on the wrong side of the $(\boldsymbol{e}_x, \boldsymbol{e}_y)$-plane and develop canes with a counter-rotating head ($\omega_z > 0$). As the migration away from the wall of cane vortices cannot be attributed to self-induction, it should be attributed to mutual induction. It is not surprising then to find counter-rotating heads all through the region of observation. It should be emphasized that the Schoppa & Hussain model is the only one (of those addressed here) which provides a logical explanation of the counter-rotating heads. The other models, as they suppose that the full cane is generated initially, give little chance for a counter-rotating head to appear, except by strong distortion of the legs or by closure of the hairpin vortices into vortex loops as suggested by Falco (1983).

It must also be mentioned that, apart from the size, the picture obtained in the logarithmic region is in good agreement with the results of Christensen & Adrian (2002). The eddy structures appear to originate at the wall, to move slowly outward, while being convected downstream at the local mean velocity.

Besides the characterization of eddy structures in the logarithmic region, the present data set, although it does not fully resolve the buffer-layer, provides some information of interest on the near-wall mechanisms. This information is gathered in figures 32 to 37 and will be summarized and discussed.

Near the wall, counter-rotating adjacent vortices are the most probable configuration in the spanwise direction, with a separation between 50^+ to 250^+. Adjacent vortices of the same sign are extremely rare. This point is, in fact, in agreement with all the models (hairpin vortices of Smith & Walker (1997), cane vortices of Hanratty & Papavassiliou (1997) and Kline & Portela (1997), alternate quasi-streamwise vortices of Schoppa & Hussain (1997)). It should nevertheless be kept in mind that the maximum value of the probability in figure 32(*a*) is of the order of 10 % which leaves room for isolated vortices of each sign. In figure 33, both low- and high-speed streaks appear closely associated with individual near-wall vortices of the appropriate sign and on the appropriate side (that is a vortex generating a sweep on a high-speed streak and an ejection on a low-speed streak). The probability of these events is not so high, suggesting the need for the construction of the complementary correlation (vortex at the fixed point and streak at the moving point), which is not available from the present data set. This picture is again in fair agreement with the models cited above, but does not contribute to the debate between hairpin and cane

vortices. To do so, the probability of having simultaneous counter-rotating vortices above a streak should be constructed.

Looking at the relation of near-wall vortices with sweeps and ejections, it was found that both ejections and sweeps are highly correlated to a nearby vortex, while the opposite correlation is less strong. This means that a near-wall vortex is required inorder to generate a sweep or ejection, but not all of them do so. Again, this point is accepted by several modellers and explicitly made, for example, by Zhou *et al.* (1999). Finally, as expected, ejections and sweeps are well correlated, respectively, with low- and high-speed streaks. The sweeps and ejections appear above the streaks. What is surprising in the present results is the shape of the correlation functions. Looking at the literature, we would expect a local extremum just above the streak and fairly localized in space. The shape observed here seems to indicate a direct vertical exchange of momentum between the near-wall region and the logarithmic region. Clearly, this point is not addressed in the literature, at least in this range of Reynolds number. Although, a clear relation is evident in the very near-wall region ($y^+ < 100$) as in the other diagrams (figures 32 to 35), this correlation is the only one to indicate a direct relation between the wall region and the outer flow.

6. Conclusion

A PIV experiment has been performed in a turbulent-boundary-layer wind tunnel. The aim of this experiment was to study the coherent structures taking part in the generation process of wall turbulence. This experiment was performed at high Reynolds number in a fairly thick boundary layer, allowing us to obtain a well-developed logarithmic region. The recording of instantaneous velocity maps in planes oriented at different angles to the flow has allowed us to characterize, with some detail, the eddy structures which develop into the logarithmic region. A sufficient number of fields were recorded in each plane to obtain statistical characteristics of these vortices (density, size and intensity). It was also possible, in the plane normal to the flow and to the wall (in the $(\boldsymbol{e}_z, \boldsymbol{e}_y)$-plane), to investigate the links between vortices, streaks, sweeps and ejections. The analysis of these results and the comparison with the existing points of view in the literature is instructive. The present results complement the existing data by providing high-Reynolds-number results. Globally, they are in fair agreement on many aspects of the flow structure with the previous experiments and the existing theories as summarized in Panton (1997). The most important conclusion from the above discussion is with regard to the low-Reynolds-number effects on wall turbulence. It seems that, in the range of relatively high Reynolds number investigated here (a well-defined log layer exists to separate the buffer layer from the wake region), the vortices which travel in the logarithmic region scale universally in wall units and keep fairly constant characteristics throughout this region. This point is somewhat different from conclusions drawn by Smith & Walker (1997), Hanratty & Papavassiliou (1997) and Kline & Portela (1997) from the studies by either DNS data or experiments at low Reynolds number. At high Reynolds number, cane vortices of the type described by Robinson (1991) appear to be born in the buffer-layer as quasi-streamwise vortices similar to those proposed by Schoppa & Hussain (2002). As observed here, they are already lifted up at an angle to the wall near 45° and they move slowly away from the wall, while being convected at the local mean velocity (see Christensen & Adrian 2002). During this travel, their size increases and intensity decreases (both slowly), keeping their circulation (ωr^2) almost constant. Thus, these

vortices appear as some flow entities from the buffer-layer that reach the logarithmic region, explaining perhaps the scaling of this region in wall units.

Among the different models investigated in the discussion, it is clear that the overall behaviour of the vortices in the logarithmic region, as deduced from the present results, is in fair agreement with the theory of Schoppa & Hussain (2002) which supposes that they are generated as quasi-streamwise vortices near the wall and not directly as arch, cane or hairpin vortices. In particular, this theory is the only one to give a logical explanation to the counter-rotating heads observed throughout the logarithmic region. It would now be of interest to investigate the wake region, to see if the tendency toward an isotropic distribution of vortices in the different planes is confirmed and to determine how the size and intensity of these vortices evolve in this region.

In the $(\boldsymbol{e}_z, \boldsymbol{e}_y)$-plane, the picture deduced from the correlation maps between the different coherent structures (vortices, streaks, ejections and sweeps) is consistent with the previous observations made mostly at low Reynolds number (see Panton 1997): sweeps are tightly linked to high-speed streaks and near-wall vortices, ejections are tightly linked to low-speed streaks and also near-wall vortices. The level of probability reached in these maps (and some of these maps themselves) leaves room for near-wall vortices generating no ejections or sweeps and streaks not directly associated with a vortex. This is consistent with the accepted model of active/inactive motions of Townsend (see Robinson 1991; Kline & Portela 1997). The agreement here is fairly close with all the results available at low Reynolds number, indicating that, in contrast to the logarithmic region, the buffer-layer appears to be less sensitive to low-Reynolds-number effects. This is of interest, as it indicates that the result of low-Reynolds-number DNS in the near-wall region are relevant for high Reynolds number and that the self-sustaining mechanism near the wall should not be so dependent (at least at first order) on the outer region. This is in agreement with a number of proposals (see Kim *et al.* 1987; Jiménez & Pinelli 1999; Schoppa & Hussain 2002; etc.). It is particularly striking that the sizes of the vortices obtained here through the logarithmic region are in fair agreement with the sizes obtained at low Reynolds number near the buffer-layer (see Hanratty & Papavassiliou 1997). If this result can be confirmed by further studies (in particular DNS at higher Reynolds number which are underway at the CTR), it means that, first the main part of the self-sustaining mechanism of wall turbulence is localized under $y^+ \simeq 100$ and second that it can be studied by DNS at a reasonable Reynolds number. This point is supported by the well-known behaviour of the mean velocity profile as a function of the Reynolds number as illustrated by figure 5: when the Reynolds number increases, only the extension outward of the logarithmic layer changes in wall scaling. This universality of the near-wall self-sustaining mechanism appears, based on the present results, extended to the range of Reynolds number investigated ($R_\theta < 19\,000$). Extrapolation to very high Reynolds number would be presently purely speculative.

Besides, the relevance of PIV for the quantitative study of turbulence and coherent structures should be emphasized. The present data, although far from being perfect, illustrate clearly that reliable and statistically relevant data can now be obtained from PIV to investigate the spatial organization of turbulence. Although the spatial resolution is limited and the measurement noise limits the range of scales accessible on the high-wavenumber side (see Foucaut & Stanislas 2002), careful use of this tool gives a deep insight into the flow organization. It is obvious from the present results that stereoscopic PIV with the largest possible CCD is an adequate tool to study turbulence organization. This is clearly illustrated by the richness of the

information gathered in the $(\boldsymbol{e}_z, \boldsymbol{e}_y)$-plane, which was the only stereoscopic one in the present study. The use of this technique in the other planes would be of strong interest and would allow us to confirm the present results and to answer a certain number of remaining open questions. The increase of the spatial resolution near the wall in the $(\boldsymbol{e}_x, \boldsymbol{e}_y)$-plane would also be of great interest. Finally, although the statistical study of turbulence with PIV is at its very beginning as compared to hot-wire anemometry, it should be mentioned that the stereoscopic dual-plane approach of Kähler & Kompenhans (2000) and Kähler & Stanislas (2000) already provides one more dimension of information, as it allows us to measure space–time correlations. This opens a wide field of investigation.

The authors are grateful to Dr J. H. Foucaut for his help in the experiments and to Dr E. Kaehler for providing the stereo PIV data.

REFERENCES

Acarlar, M. S. & Smith, C. R. 1987*a* A study of hairpin vortices in a laminar boundary layer. Part 1. Hairpin vortices generated by a hemisphere protuberance. *J. Fluid Mech.* **175**, 1–41.

Acarlar, M. S. & Smith, C. R. 1987*b* A study of hairpin vortices in a laminar boundary layer. Part 2. Hairpin vortices generated by fluid injection. *J. Fluid Mech.* **175**, 43–83.

Adrian, R. J. 1991 Particle-imaging techniques for experimental fluid mechanics. *Annu. Rev. Fluid Mech.* **23**, 1–54.

Adrian, R. J., Christensen, K. T. & Liu, Z. C. 2000*a* Analysis and interpretation of turbulent velocity fields. *Exps. Fluids* **29**, 275–290.

Adrian, R. J., Meinhart, C. D. & Tomkins, C. D. 2000*b* Vortex organization in the outer region of the turbulent boundary layer. *J. Fluid Mech.* **422**, 1–54.

Blackwelder, R. F. & Kaplan, R. E. 1976 On the wall structure of turbulent boundary layer. *J. Fluid Mech.* **76**, 89–112.

Blackwelder, R. F. & Eckelmann, H. 1979 Streamwise vortices associated with the bursting phenomenon. *J. Fluid Mech.* **94**, 577–594.

Bonnet, J. P., Delville, J., Glauser, M. N., Antonia, R. A., Bisset, D. K., Cole, D. R., Fiedler, H. E., Garem, J. H., Hilberg, D., Jeong, J., Kevlahan, N. K. R., Ukeiley, L. S. & Vincendeau, E. 1998 Collaborative testing of eddy structure identification methods in free turbulent shear flows. *Exps. Fluids* **25**, 197–225.

Camussi, R. 2002 Coherent structure identification from wavelet analysis of particle image velocimetry data. *Exps. Fluids* **32**, 76–86.

Carlier, J. 2001 Étude des structures cohérentes de la turbulence de paroi à grand nombre de Reynolds par vélocimétrie par images de particules. Thèse de Doctorat 2959, Université des Sciences et Technologies de Lille, France.

Christensen, K. T. & Adrian, R. J. 2002 The velocity and acceleration signatures of small-scale vortices in turbulent channel flow. *J. Turbulence* **3**.

Corino, E. R. & Brodkey, R. S. 1969 A visual investigation of the wall region in turbulent flow. *J. Fluid Mech.* **37**, 1–30.

DeGraaff, D. B. & Eaton J. K. 2000 Reynolds number scaling of the flat plate turbulent boundary layer. *J. Fluid Mech.* **422**, 319–346.

Del Alamo, J. C. & Jimenez, J. 2003 Spectra of very large anisotropic scales in turbulent channels. *Phys. Fluids* **15**, L41–L44.

Erm, L. P. & Joubert, P. N. 1991 Low-Reynolds-number turbulent boundary layers. *J. Fluid Mech.* **230**, 1–44.

Falco, R. E. 1974 Some comments on turbulent boundary layer structure inferred from the movements of passive contaminant. *AIAA Paper* 74-99.

Falco, R. E. 1983 New results a review and synthesis of the mechanism of turbulence production in boundary layers and its modification. *AIAA Paper* 83-0377.

Foucaut, J. M., Carlier, J. & Stanislas, M. 2000 Post-processing of PIV records to allow derivative computation. *10th Intl Symp. on Applic. of Laser Technol. to Fluid Mech. Lisbon, Portugal.*

Foucaut, J. M. & Stanislas, M. 2002 Some considerations on the accuracy and frequency response of some derivative filters applied to particle image velocimetry vector fields. *Meas. Sci. Technol.* **13**, 1058–1071.

Gilliot-Ottavy, A. 1997 Caractérisation par anémométrie à fils chauds d'écoulements turbulents de Poiseuille et de Couette–Poiseuille en vue de la validation de modèles de turbulence. Thèse de Doctorat 2146, Université des Sciences et Technologies de Lille, France.

Hanratty, T. J. & Papavassiliou, D. V. 1997 The role of wall vortices in producing turbulence. *Self-Sustaining Mechanisms of Wall Turbulence* (ed. R. L. Panton), pp. 83–108. Computational Mechanics.

Head, M. R. & Bandyopadhyay, P. 1981 New aspects of turbulent boundary layer structure. *J. Fluid Mech.* **107**, 297–338.

Hinze, J. O. 1975 *Turbulence*, 2nd edn. McGraw-Hill.

Hoyez-Delaliaux, M. C. 1990 Etude des caractéristiques instationnaires d'une couche limite turbulente de plaque plane sans gradient de pression. Thèse de Doctorat 610, Université des Sciences et Technologies de Lille, France.

Jeong, J. & Hussain, F. 1995 On the identification of a vortex. *J. Fluid Mech.* **285**, 69–94.

Jiménez, J. & Pinelli, A. 1999 The autonomous cycle of near-wall turbulence. *J. Fluid Mech.* **389**, 335–359.

Kähler, C. J., Adrian, R. J. & Willert, C. E. 1998 Turbulent boundary layer investigations with conventional and stereoscopic PIV. *9th Intl Symp. on Applic. of Laser Technol. to Fluid Mech. Lisbon, Portugal.*

Kähler, C. J. & Kompenhans, J. 2000 Fundamentals of multiple plane stereo particle image velocimetry. *Exps. Fluids* **29**, S070–S077.

Kähler, C. J. & Stanislas, M. 2000 Investigation of wall bounded flows by means of multiple plane stereo PIV. *10th Intl Symp. on Applic. of Laser Technol. to Fluid Mech. Lisbon, Portugal.*

Keane, R. D. & Adrian, R. J. 1992 Theory of cross-correlation analysis of PIV images. *Appl. Sci. Res.* **49**, 191–215.

Kim, H. T., Kline, S. J. & Reynolds, W. C. 1971 The production of turbulence near a smooth wall in a turbulent boundary layer. *J. Fluid Mech.* **50**, 133–160.

Kim, J., Moin, P. & Moser, R. 1987 Turbulence statistics in fully developed channel flow at low Reynolds number. *J. Fluid Mech.* **177**, 133–166.

Klebanoff, P. S. 1955 Characteristics of turbulence in a boundary layer with zero pressure gradient. *NACA Rep.* 1247, 1135–1153.

Klewicki, J. & Falco, R. 1996 Spanwise vorticity structure in turbulent boundary layer. *Intl J. Heat and Fluid Flow* **17**, 363–376.

Klewicki, J. & Falco, R. 1990 On accurately measuring statistics associated with small-scale structure in turbulent boundary layers using hot-wire probes. *J. Fluid Mech.* **219**, 119–142.

Kline, S. J. & Portela, L. M. 1997 A view of the structure of turbulent boundary layers. *Self-Sustaining Mechanisms of Wall Turbulence* (ed. R. L. Panton), pp. 167–180. Computational Mechanics.

Kline, S. J., Reynolds, W. C., Schraub, F. A. & Runstadler, P. W. 1967 The structure of turbulent boundary layers. *J. Fluid Mech.* **30**, 741–773.

Lecordier, B. 1997 Étude de l'interaction de la propagation d'une flamme prémélangée avec le champ aerodynamique, par association de la tomographie laser et de la vélocimétrie par images de particule. Thèse de Doctorat Faculté des Sciences de l'Université de Rouen, France.

Liu, Z., Adrian, R. J. & Hanratty, T. J. 2001 Large-scale modes of turbulent channels flow: transport and structure. *J. Fluid Mech.* **448**, 53–80.

Liu, Z. C., Adrian, R. J., Meinhart, C. D. & Lai, W. 1996 Visualisation of structure in a turbulent boundary layer using a stereoscopic particle image velocimetry. *8th Intl Symp. on Applic. of Laser Technol. to Fluid Mech. Lisbon, Portugal.*

Marusic I. & Kungel G. J. 2003 Streamwise turbulence intensity formulation for flat plate boundary layers. *Phys. Fluids* **15**, 2461–2464.

Meinhart, C. D. 1994 Investigation of boundary-layer structure using particle image velocimetry. PhD dissertation, University of Illinois, Urbana, Illinois, USA.

Meinhart, C. D. & Adrian, R. J. 1995 Measurement of the zero-pressure gradient turbulent boundary layer using particle image velocimetry. *AIAA Paper* 95-0789.

Mellor, G. L. 1966 The effects of pressure gradients on turbulent flow near a smooth wall. *J. Fluid Mech.* **24**, 255–274.

Ong, L. & Wallace, J. M. 1998 Joint probability density analysis of the structure and dynamics of the vorticity field of a turbulent boundary layer. *J. Fluid Mech.* **367**, 291–328.

Panton, R. L. 1997 *Self-Sustaining Mechanisms of Wall Turbulence*. Computational Mechanics.

Panton, R. L. 1999 Self-sustaining mechanisms of wall turbulence – a review. *AIAA Paper* 99-0552.

Rajagopalan, S. & Antonia, R. 1993 Structure of the velocity field associated with the spanwize vorticity in the wall region of a turbulent boundary layer. *Phys. Fluids* A **5**, 2502–2510.

Robinson, S. K. 1991 Coherent motions in the turbulent boundary layer. *Annu. Rev. Fluid Mech.* **23**, 601–639.

Scarano, F., Benocci, C. & Riethmuller, M. L. 1999 Pattern-recognition analysis of the turbulent flow past a backward facing step. *Phys. Fluids* **11**, 3808–3818.

Scarano, F. 2002 Iterative image deformation methods in PIV. *Meas. Sci. Technol.* **13**, R1–R19.

Schoppa, W. & Hussain, F. 1997 Genesis and dynamics of coherent structures in near-wall turbulence: a new look. *Self-Sustaining Mechanisms of Wall Turbulence* (ed. R. L. Panton), pp. 385–422. Computational Mechanics.

Schoppa, W. & Hussain, F. 2002 Coherent structure generation in near-wall turbulence. *J. Fluid Mech.* **453**, 57–108.

Schram, C. & Riethmuller, M. L. 2000 Temporal evolution of coherent structures in a starting jet flow using DPIV and continuous wavelet analysis. *Euromech 411, Rouen, France.*

Smith, C. R. & Walker, J. D. A. 1997 Sustaining mechanisms of turbulent boundary layers: the role of vortex development and interactions. *Self-Sustaining Mechanisms of Wall Turbulence* (ed. R. L. Panton), pp. 13–48. Computational Mechanics.

Spalart, P. R. 1988 Direct simulation of a turbulent boundary layer up to $R_\theta = 1410$. *J. Fluid Mech.* **187**, 61–98.

Theodorsen, T. 1952 Mechanism of turbulence. *Proc. Midwest. Conf. Fluid Mech. Colombus, Ohio*, 2nd edn, pp. 1–18.

Townsend, A. A. 1976 The Structure of Turbulent Shear Flows, 2nd edn. Cambridge University Press.

Wallace, J. M., Eckelmann, H. & Brodkey, R. S. 1972 The wall region in turbulent shear flow. *J. Fluid Mech.* **54**, 39–48.

Westerweel, J. 1997 Fundamentals of digital particle image velocimetry. *Meas. Sci. Technol.* **8**, 1379–1392.

Willmarth, W. W. & Lu, S. S. 1972 Structure of the Reynolds stress near a wall. *J. Fluid Mech.* **55**, 65–92.

Zhou, J., Adrian, R. J., Balachandar, S. & Kendall, T. M. 1999 Mechanisms for generating coherent packets of hairpin vortices in channel flow. *J. Fluid Mech.* **387**, 353–396.